Density Functional Study on Geometrical Features and Electronic Structures of Di-μ-oxo-Bridged $[Mn_2O_2(H_2O)_8]^{q+}$ with Mn(II), Mn(III), and Mn(IV)

Masaki Mitani,* Yohei Wakamatsu, Takeharu Katsurada, and Yasunori Yoshioka*

Division of Chemistry for Materials, Graduate School of Engineering, Mie University, Kurima-machiya, Tsu, Mie 514-8507, Japan

Received: December 9, 2005; In Final Form: October 5, 2006

We report the geometrical features and electronic structures of di-μ-oxo-bridged Mn−Mn binuclear complexes with H_2O ligands $[Mn_2O_2(H_2O)_8]^{q+}$ in the iso- and mixed-valence oxidation states. All of the combinations among Mn(II), Mn(III), and Mn(IV) ions are considered the oxidation states of the Mn−Mn center, and the changes in molecular structure induced by the different electron configurations of Mn-based orbitals are investigated in relation to the oxygen-evolving complex (OEC) of photosystem II. The stable geometries of complexes are determined by using the hybrid-type density functional theory for both of the highest- and lowest-spin couplings between Mn sites, and the lowest-spin-coupled states are energetically more favorable than the highest-spin-coupled states except in the case of the complexes with the Mn(II) ion. The coordination positions of H_2O ligands at the Mn(II) site tend to shift from the octahedral positions in contrast to those at the Mn(III) and Mn(IV) sites. The shape of the Mn_2O_2 core and the distances between the Mn ions and the H_2O ligands vary depending on the electron occupations of the octahedral e_g orbitals on the Mn site with an antibonding nature for the Mn−ligand interactions, indicating the trend as Mn(II)−O > Mn(III)−O and Mn(IV)−O, O−Mn(II)−O > O−Mn(III)−O > O−Mn(IV)−O among the iso-valence Mn_2O_2 cores, and O−Mn(lower)−O < O−Mn(higher)−O within the mixed-valence Mn_2O_2 core, and as Mn(II)−OH_2 and Mn(III)−OH_2 > Mn(IV)−OH_2 for the axial H_2O ligand. The optimized geometries of model complexes are compared with the X-ray structure of the OEC, and it is suggested that the cubanelike Mn cluster of the active site may not contain a Mn(II) ion. The effective exchange integrals are estimated by applying the approximate spin projection to clarify the magnetic coupling between Mn sites, and the superexchange pathways through the di-μ-oxo bridge are examined on the basis of the singly occupied magnetic orbitals derived from the singlet-coupled natural orbitals in the broken-symmetry state. The comparisons of the calculated results between $[Mn_2O_2(H_2O)_8]^{q+}$ in this study and $[Mn_2O_2(NH_3)_8]^{q+}$ reported by McGrady et al. suggest that the symmetric pathways are dominant to the exchange coupling constant, and the crossed pathway would be less important for the former than it would for the latter in the Mn(III)−Mn(III), Mn(IV)−Mn(IV), and Mn(III)−Mn(IV) oxidation states.

I. Introduction

Photosynthetic water oxidation in photosystem II (PSII) takes place at the tetranuclear Mn cluster as an active site, and the functional unit including the Mn cluster is referred to as the oxygen-evolving complex (OEC) or water-oxidizing complex (WOC). The oxidation reaction from water to dioxygen molecules is catalyzed by the OEC as $2H_2O \rightarrow O_2 + 4e^- + 4H^+$. Several models for the reaction mechanism of water oxidation or for the molecular structure of the OEC have been proposed by experimental and theoretical studies, and many related articles have been published (e.g., refs 1−16).

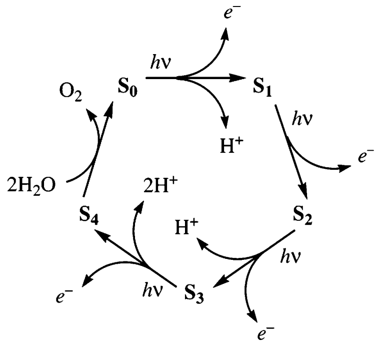

Figure 1. S-state catalytic cycle of water oxidation by the OEC.

The reaction cycle of water oxidation by the OEC has been known as the S-state catalytic cycle or the Kok cycle, in which the oxidation reaction proceeds through the five-step process from the S_0 state to the S_4 state. Figure 1 shows the S-state catalytic cycle schematically.[1] The tetranuclear Mn cluster of the active site has been considered to be oxidized stepwise with releasing the electrons and protons through each of the oxidation steps as indicated in Figure 1, then molecular dioxygen would be produced in the last step from the S_4 state to the S_0 state. The oxidation states of the four Mn ions at the reaction center in each of the S states have been suggested, for example, as Mn_4(II, III, IV, IV) in the S_0 state → Mn_4(III,III,IV,IV) in the S_1 state → Mn_4(III,IV,IV,IV) in the S_2 state → Mn_4(III,IV,IV,IV) with the μ-oxo radical in the S_3 state → Mn_4(III,IV,IV,IV) in the S_4 state,[1] and the iso- and mixed-valence Mn−Mn pairs would appear in the S-state catalytic cycle. The

---

* To whom correspondence should be addressed. M.M.: phone: +81-59-231-9256; fax: +81-59-231-9742; e-mail: mitani@chem.mie-u.ac.jp. Y.Y.: phone: +81-59-231-9742; fax: +81-59-231-9742; e-mail: yyoshi@chem.mie-u.ac.jp.

10.1021/jp0571877 CCC: $33.50

extended X-ray absorption fine structure (EXAFS) and electron spin-echo envelope modulation (ESEEM) spectroscopy have indicated that the first-shell ligands of the Mn cluster are mostly oxygens, one or two nitrogens, and possibly one chlorine. The dimer complex of di-μ-oxo-bridged Mn−Mn binuclear centers linked to each other by a mono-μ-oxo bridge has been proposed as the working model for the tetranuclear Mn cluster in the OEC on the basis of the available experimental results.[1]

X-ray crystallographic studies of PSII have been reported in recent years.[17−21] Although the 3D coordinates obtained by several experiments are available from the Protein Data Bank (PDB), the observed structures of the Mn cluster in the OEC are different from each other. The crystal structures from *Synechococcus elongatus* at 3.8 Å resolution,[17] *Thermosynechococcus vulcanus* at 3.7 Å resolution,[18] and *Thermosynechococcus elongatus* at 3.2 Å resolution[20] suggest a Y-shaped arrangement of the Mn ions, in which any Ca ions were not detected[17,18] or only four metal ions were accommodated.[20] However, the crystal structure from *Thermosynechococcus elongatus* at 3.5 Å resolution[19] strongly indicated the cubanelike arrangement of Mn and Ca ions with μ-oxo bridges, such as Mn_3CaO_4, in which the details of the surrounding coordination sphere around the Mn cluster were also assigned. Thus, the cubanelike models for the reaction mechanism of water oxidation by the OEC are now widely discussed.[22−27] However, more recently, the X-ray structure of PSII from *Thermosynechococcus elongates* at 3.0 Å resolution has been reported,[21] in which the Mn cluster was best approximated by the hook-shaped arrangement of Mn ions resembling the Y-shaped structure. The position of the Ca ion was suggested as the vertex of a trigonal pyramid formed by the Mn1, Mn2, and Mn3 ions numbered from the highest electron-density, and the Mn4 ion was linked to the Mn3 ion. The Mn−Mn distances were estimated to be about 2.7 Å for Mn1−Mn2 and Mn2−Mn3 and about 3.3 Å for Mn1−Mn3 and Mn3−Mn4, and it was suggested that the Mn−Mn pairs with shorter and longer separations are connected by di-μ-oxo and mono-μ-oxo bridges, respectively, although the positions of μ-oxo ions were not reported. The Mn−Ca distances forming the trigonal pyramid were indicated to be equidistant for the Mn1, Mn2, and Mn3 ions at about 3.4 Å.

Although several experimental structures of the Mn cluster in the OEC are available as described above, the detailed 3D geometry has not yet been determined crystallographically because of the low resolution of the X-ray structures. Therefore, computational investigations of geometrical features and electronic structures for model complexes are important to examine water oxidation by the OEC, and we studied the basic unit of the Mn_2O_2 face constructing the cubanelike Mn cluster reported in ref 19 in this work. Figure 2 shows the observed X-ray structure of the cubanelike Mn cluster in the OEC (pdb code: 1S5L). Three Mn ions and one Ca ion form the cubanelike structure by tri-μ-oxo bridges, and the outer Mn ion is linked to Mn_3CaO_4 in part by a mono-μ-oxo bridge, in which the Mn−Mn distances were reported to be about 2.7 Å within the cubanelike cluster and about 3.3 Å between the cubanelike cluster and the outer ion, whereas the Mn−Ca distance was reported to be about 3.4 Å.

In the field of computational chemistry, quantum chemical calculations have been carried out for several models or synthetic compounds of the Mn complex with μ-oxo bridges in relation to the Mn cluster in the OEC.[28−38] Regarding the studies of the di-μ-oxo-bridged Mn dimer using the broken-symmetry DFT method, the magnetic interactions of $[Mn_2O_2(pic)_4]$ (picH = picolinic acid) and $[Mn_2O_2X_8]^{q+}$ (X = H^-, F^-, Cl^-, H_2O, and NH_3) were examined in ref 32, the redox-induced changes in molecular geometry and magnetic properties of $[Mn_2O_2(NH_3)_8]^{q+}$ were investigated in ref 30, and the geometrical parameters and electronic structures of $[Mn_2O_2(NH_3)_6(H_2O)_2]^{q+}$ were reported in refs 34 and 37. Theoretical examinations of the cubanelike model using the X-ray structure were recently attempted for the oxidation states in the S-state catalytic cycle,[39,40] and the spin structures with noncollinear spin alignment were predicted by applying the Hartree−Fock calculation using general spin orbitals (GSO-HF) in ref 40. However, the geometrical structures and electron configurations of the S_0−S_4 states for the cubanelike Mn cluster in the OEC have not yet been clarified from a theoretical viewpoint.

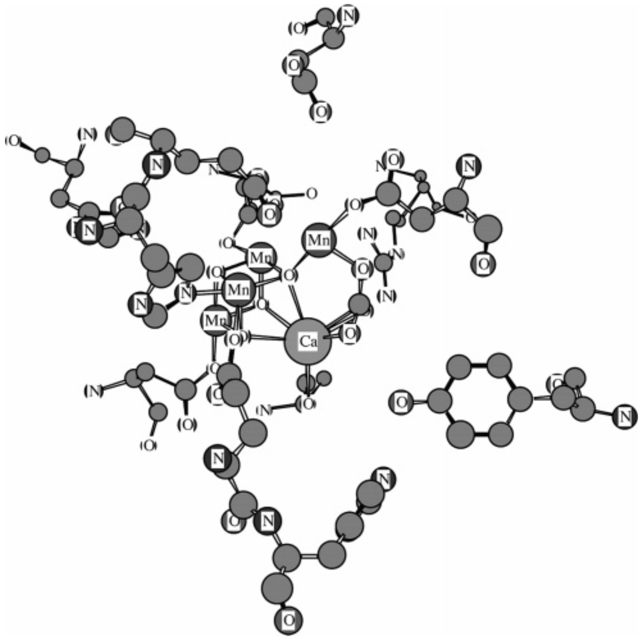

Figure 2. X-ray structure of the cubanelike Mn cluster in the OEC (pdb code: 1S5L).[19] The atoms without an element symbol indicate carbon atoms.

In the previous paper,[41] we investigated the geometrical and electronic structures of model complexes $[Mn_2O_2(H_2O)_8]^{q+}$ (q = 0, 2, 4) using the hybrid-type density functional theory (DFT) as the first step toward a theoretical examination of the reaction mechanism for water oxidation by the OEC. The stable geometries of energy minima were respectively determined for each of the highest- and lowest-spin states by applying the LanL2DZ[42] effective core potential (ECP) to the Mn ions, and the relative stabilities, charge and spin distributions, and electron configurations in the Mn(II)−Mn(II), Mn(III)−Mn(III), and Mn(IV)−Mn(IV) oxidation states were reported. However, the atomic charges on the oxidized Mn ions obtained from the ECP method seemed to be too small. Therefore, the model complexes should be re-examined using the all-electron DFT method.

In the present article, we study the geometrical characteristics of model complexes $[Mn_2O_2(H_2O)_8]^{q+}$ (q = 0−4) and their changes depending on the oxidation state of the Mn−Mn center by using the all-electron hybrid-type DFT calculation. The highest- and lowest-spin couplings between the Mn sites are considered in the Mn−Mn center. The iso- and mixed-valence combinations among Mn(II), Mn(III), and Mn(IV) ions, the iso-valence centers of Mn(II)−Mn(II), Mn(III)−Mn(III), and Mn(IV)−Mn(IV) and the mixed-valence centers of Mn(II)−Mn(III), Mn(II)−Mn(IV), and Mn(III)−Mn(IV), and the relative stabilities of both spin alignments in each oxidation state are examined. The Mn_2O_2 geometries of the optimized complexes are com-

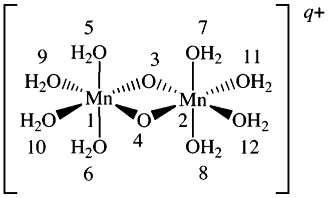

Figure 3. Model complex with a di-μ-oxo bridged Mn−Mn binuclear center and numbering of Mn_2O_2 atoms and H_2O molecules.

pared with the X-ray structure of the cubanelike Mn_3CaO_4 cluster in the OEC. The distributions of charge and spin densities in the complexes are evaluated using the Mulliken population analysis, and the singly occupied electron configurations of the Mn−Mn centers are elucidated using the natural orbital analysis. The magnetic interactions between Mn sites are estimated in terms of the effective exchange integrals and superexchange pathways mediated by the μ-oxo bridge. The calculated structures, electron populations, and magnetic properties of $[Mn_2O_2(H_2O)_8]^{q+}$ in this study are compared with those of $[Mn_2O_2(NH_3)_8]^{q+}$ given in ref 30.

II. Model Complex and Computational Method

Because the di-μ-oxo-bridged Mn−Mn center forms the Mn_2O_2 faces of the cubanelike Mn cluster in the OEC as shown in Figure 2 and it has been considered that only two of the four Mn sites may be sensitive to a photooxidation reaction of water molecules in many of earlier models, we study the Mn−Mn binuclear complexes bridged by di-μ-oxo ions $[Mn_2O_2(H_2O)_8]^{q+}$ shown in Figure 3 as a simplified model of the tetranuclear Mn cluster in the OEC. Eight H_2O molecules are placed around Mn ions as ligands to form the six-coordinated Mn sites. We respectively take the Mn−Mn and O−O axes as the *y* and *x* axes, and the *z* axis is perpendicular to the plane formed by the Mn_2O_2 core facing the axial direction. Therefore, two octahedral e_g orbitals at each Mn site include the *xy* (equatorial) and z^2 (axial) components of the 3d orbital, respectively. In this article, we apply the following numbering of atoms and molecules to the model complexes: the Mn_2O_2 atoms, axial H_2O molecules, and equatorial H_2O molecules are respectively numbered from 1 to 4, from 5 to 8, and from 9 to 12 as indicated in Figure 3. It is noted that the Mn1 and Mn2 ions, respectively, correspond to the Mn ions in lower and higher oxidation states of a mixed-valence Mn−Mn pair in the case of mixed-valence complexes.

In the S-state catalytic cycle, the iso- and mixed-valence states of Mn−Mn pairs are generated through the oxidation steps. We consider the possible iso- and mixed-valence combinations of Mn(II), Mn(III), and Mn(IV) ions as the Mn−Mn center of complexes as follows: Mn(II)−Mn(II) (**1**), Mn(III)−Mn(III) (**2**), and Mn(IV)−Mn(IV) (**3**) for the iso-valence complexes; Mn(II)−Mn(III) (**4**), Mn(II)−Mn(IV) (**5**), and Mn(III)−Mn(IV) (**6**) for the mixed-valence complexes. The formal charges of the Mn and μ-oxo ions are respectively taken as 2+ for Mn(II), 3+ for Mn(III), and 4+ for Mn(IV) and as 2− for μ-oxo, by which the total charge *q* of each complex is given as 0 for **1**, 1 for **4**, 2 for **2** and **5**, 3 for **6**, and 4 for **3**. The highest- and lowest-spin couplings between locally parallel-spin alignments at each of the two Mn ions are applied to specify the electronic states of the complexes. The formal 3d electron occupations of Mn ions are thus open shell with the parallel spins as $3d^5$ for Mn(II), $3d^4$ for Mn(III), and $3d^3$ for Mn(IV), and the locally parallel spins on the Mn(II), Mn(III), and Mn(IV) centers are coupled with the same and opposite directions between two Mn sites, respectively, in the highest- and lowest-spin configurations. These spin couplings lead to the total spin *S* of $^{10}/_2$ for **1**, $^9/_2$ for **4**, $^8/_2$ for **2** and **5**, $^7/_2$ for **6**, and $^6/_2$ for **3** in the highest-spin configurations, whereas the total spin *S* is $^0/_2$ for **1**−**3**, $^1/_2$ for **4** and **6**, and $^2/_2$ for **5** in the lowest-spin configurations.

The unrestricted hybrid-type DFT method using the B3LYP combination of exchange and correlation functionals (UB3LYP)[43,44] was applied to the full geometry optimization of model complexes under no spatial symmetry constraints. The optimized stationary points were confirmed to be or not to be energy minimums using the vibrational frequency analysis. The Ahlrichs VDZ,[45] Pople 6-31G(d),[46] and Pople 6-31G[46] sets were employed as the basis functions of the Mn, O, and H species, respectively. The lowest-spin configurations were obtained as broken-symmetry solutions. The Mulliken population analysis was used to evaluate the distributions of charge and spin densities. All the results given in this article were calculated using the Gaussian 98 program package.[47]

III. Effective Exchange Integral and Magnetic Orbital

The effective exchange integral represents the magnitude of magnetic interactions between spin sites, and the positive or negative value respectively corresponds to the parallel (ferromagnetic) or antiparallel (antiferromagnetic) spin coupling. Several approximation schemes to calculate the effective exchange integral by employing the broken-symmetry approach have been proposed.[48−51]

The Heisenberg spin Hamiltonian is used for the iso-valence binuclear complexes with localized spins,

$$\hat{H} = -2J\,\vec{S}_a \cdot \vec{S}_b \tag{1}$$

where *J* is the effective exchange integral (exchange coupling constant) between the *a*th and *b*th metal sites with spin vectors $\vec{S}_a$ and $\vec{S}_b$. Three-types of approximation are applicable to obtain the *J* value,[48−50]

$$J^{(1)} = \frac{{}^{LS}E - {}^{HS}E}{{S_{max}}^2} \tag{2}$$

$$J^{(2)} = \frac{{}^{LS}E - {}^{HS}E}{S_{max}(S_{max} + 1)} \tag{3}$$

$$J^{(3)} = \frac{{}^{LS}E - {}^{HS}E}{{}^{HS}\langle \hat{S}^2 \rangle - {}^{LS}\langle \hat{S}^2 \rangle} \tag{4}$$

where ${}^{LS}E$ and ${}^{HS}E$ represent the total energies of the low- and high-spin states, respectively, with the expectation values of total spin angular momentum ${}^{LS}\langle \hat{S}^2 \rangle$ and ${}^{HS}\langle \hat{S}^2 \rangle$.

A more general spin Hamiltonian including the resonance delocalization (double exchange) effects is used for the mixed-valence binuclear complexes,

$$\hat{H} = -2J\vec{S}_a \cdot \vec{S}_b \pm B\left(S + \frac{1}{2}\right) \tag{5}$$

where *B* is the resonance delocalization parameter.[52] The *J* value is approximated by two schemes using the average energy of two delocalized high-spin states denoted as g and u, in which an extra electron is placed in the delocalized orbitals with the in-phase and out-of-phase combinations of specific (unpaired) metal 3d orbitals, respectively,[48,51]

$$B = \frac{{}^{\mathrm{HS}}E_{\mathrm{u}} - {}^{\mathrm{HS}}E_{\mathrm{g}}}{2S_{\max} + 1} \qquad (6)$$

$$J^{(4)} = \frac{{}^{\mathrm{LS}}E - {}^{\mathrm{HS}}E_{\mathrm{av}}}{\left(S_{\max} + \frac{1}{2}\right)\left(S_{\max} - \frac{1}{2}\right)} \qquad (7)$$

$$J^{(5)} = \frac{{}^{\mathrm{LS}}E - {}^{\mathrm{HS}}E_{\mathrm{av}}}{{}^{\mathrm{HS}}\langle \hat{S}^2 \rangle_{\mathrm{av}} - {}^{\mathrm{LS}}\langle \hat{S}^2 \rangle} \qquad (8)$$

$$^{\mathrm{HS}}E_{\mathrm{av}} = \frac{{}^{\mathrm{HS}}E_{\mathrm{g}} + {}^{\mathrm{HS}}E_{\mathrm{u}}}{2} \qquad (9)$$

$$^{\mathrm{HS}}\langle \hat{S}^2 \rangle_{\mathrm{av}} = \frac{{}^{\mathrm{HS}}\langle \hat{S}^2 \rangle_{\mathrm{g}} + {}^{\mathrm{HS}}\langle \hat{S}^2 \rangle_{\mathrm{u}}}{2} \qquad (10)$$

It is noted that eqs 4 and 8 are derived from the approximate spin projection method developed by Yamaguchi et al.[49−51] Because we have confirmed that eqs 2−4 or eqs 7 and 8 give similar J values for $[\mathrm{Mn_2O_2(H_2O)_8}]^{q+}$ in this study (the $|J|$ values obtained from eq 3 are somewhat smaller than those obtained from eq 2 or eq 4), only the calculated J values of $[\mathrm{Mn_2O_2(H_2O)_8}]^{q+}$ using eq 4 or eq 8 are reported in this article.

The natural orbitals and their electron occupation numbers are obtained by diagonalizing the first-order reduced density matrix as the eigenvectors and eigenvalues, respectively,

$$\rho(r, r') = \sum_i n_i \phi_i(r)\, \phi_i^*(r') \qquad (11)$$

The pair of natural orbitals ϕ_{b} (bonding) and ϕ_{a} (antibonding) forming a singlet biradical in the broken-symmetry state can be specified by their electron occupation numbers, which give 2.0 as the sum of n_{b} and n_{a}. The natural orbitals delocalized over two spin sites are related to the magnetic orbitals localized around one of the spin sites as follows,

$$\psi^{\pm} = \sqrt{\frac{n_{\mathrm{b}}}{2}}\phi_{\mathrm{b}} \pm \sqrt{\frac{n_{\mathrm{a}}}{2}}\phi_{\mathrm{a}} \qquad (12)$$

By using eq 12, it is possible to transform the symmetry-adapted natural orbitals of a singlet biradical pair into the broken-symmetry magnetic orbitals after applying the plus and minus mixing with their electron occupation numbers as the weighting factors. In this article, the superexchange pathways between Mn sites through the di-μ-oxo bridge in $[\mathrm{Mn_2O_2(H_2O)_8}]^{q+}$ are examined on the basis of the magnetic orbitals.

The electron population on atom X is given as follows under the Mulliken partitioning,

$$P^{\mathrm{X}} = \sum_i n_i \sum_r^{\text{on X}} \Big(\sum_s^{\text{all}} C_{ri} C_{si} S_{rs}\Big) = \sum_i n_i \sum_r^{\text{on X}} P_{ri} = \sum_i P_i^{\mathrm{X}} \qquad (13)$$

$$\sum_r^{\text{all}} P_{ri} = \sum_r^{\text{all}} \sum_s^{\text{all}} C_{ri} C_{si} S_{rs} = \langle \psi_i | \psi_i \rangle = 1 \qquad (14)$$

TABLE 1: Total and Relative Energies of Iso- and Mixed-Valence Complexes $[\mathrm{Mn_2O_2(H_2O)_8}]^{q+}$

complex	S	$\langle S^2 \rangle$	total energy (au)	relative energy (kcal/mol)
1	10/2	30.00	−3063.71090	0.16
	0/2	4.99	−3063.71117	0.00
2	8/2	20.09	−3063.23663	7.06
	0/2	4.01	−3063.24788	0.00
3	6/2	12.19	−3061.99682	2.78
	0/2	3.02	−3062.00126	0.00
4a	9/2	24.80	−3063.54666	0.63
	1/2	4.77	−3063.54765	0.00
4b	9/2	24.80	−3063.54624	0.89
	1/2	4.78	−3063.54719	0.29
5	8/2	20.05	−3063.21126	0.09
	2/2	4.99	−3063.21140	0.00
6	7/2	15.88	−3062.72489	5.65
	1/2	3.76	−3062.73390	0.00

where C_{ri} and C_{si} denote the expansion coefficients for the rth and sth basis functions in the ith molecular orbital and S_{rs} indicates the overlap integral between the rth and sth basis functions. The atomic population P^{X} is obtained as the sum of contributions from each molecular orbital P_i^{X}, and P_{ri} is the gross orbital population of the rth basis function in the ith molecular orbital, representing the contribution of the rth basis function to P_i^{X} or the weight of the rth basis function for electron distribution in the ith molecular orbital. In this article, we use the P_{ri} values (multiplied by 100) as the composition of the molecular orbitals.

IV. Relative Stability of Model Complex

We found several energy minima of model complexes with similar or different locations of $\mathrm{H_2O}$ ligands in different orientations except in **1**. The energy intervals from the most stable structure were obtained as follows for the lowest-spin configurations: 0.1 and 0.7 kcal/mol for **2** and **3**; 0.3, 4.0, 6.6, 7.7, and 10.3 kcal/mol for **4**; 0.9, 2.5, and 5.5 kcal/mol for **5**; 1.9 kcal/mol for **6**. The relative stabilities among energy minima of iso-valence complexes **2** and **3** with similar $\mathrm{H_2O}$ positions are almost equivalent (within 1 kcal/mol), whereas some of the energy minima for mixed-valence complexes **4**−**6** with different $\mathrm{H_2O}$ positons indicate a relatively large instability (more than 5 kcal/mol). Hereafter in this article, we focus our attention on the most-stable energy minima of complexes **1**−**6**, and complex **4** has two most-stable energy minima with different coordination patterns of $\mathrm{H_2O}$ ligand.

It is noted that the structures of the ECP energy minima for **2** that were reported in the previous study[41] became the third-order saddle points with three imaginary frequencies by the all-electron calculations as follows: 142.3i, 102.1i, and 84.6i $\mathrm{cm^{-1}}$ (highest-spin configuration); 152.6i, 110.6i, and 94.6i $\mathrm{cm^{-1}}$ (lowest-spin configuration). The all-electron method predicted three energy minima with geometries that differ from the ECP geometries. However, energy minima with similar structures were obtained by the ECP and all-electron methods for **1** and **3**.

We summarize the total and relative energies of iso- and mixed-valence complexes in Table 1 together with the expectation values of total spin angular momentum. The different energy minima of **4** with near energies are distinguished by alphabetical symbols as **4a** and **4b**.

The expectation values of total spin angular momentum $\langle \hat{S}^2 \rangle$ are obtained as 30.00 for **1** with $S = {}^{10}/_{2}$, 20.09 for **2** with $S = {}^{8}/_{2}$, 12.19 for **3** with $S = {}^{6}/_{2}$, 24.80 for **4a** and **4b** with $S = {}^{9}/_{2}$, 20.05 for **5** with $S = {}^{8}/_{2}$, and 15.88 for **6** with $S = {}^{7}/_{2}$ (highest-spin configurations) and as 4.99 for **1** with $S = {}^{0}/_{2}$, 4.01 for **2** with $S = {}^{0}/_{2}$, 3.02 for **3** with $S = {}^{0}/_{2}$, 4.77 and 4.78 for **4a** and **4b** with $S = {}^{1}/_{2}$, 4.99 for **5** with $S = {}^{2}/_{2}$, and 3.76 for **6** with $S = {}^{1}/_{2}$ (lowest-spin configurations). It is suggested from these results of $\langle \hat{S}^2 \rangle \approx S(S+1)$ for the highest-spin configurations and $\langle \hat{S}^2 \rangle \approx S(S+1) + 5$ (**1**), 4 (**2**, **4a**, and **4b**), and 3 (**3**, **5**, and **6**) for the lowest-spin configurations that the highest-spin

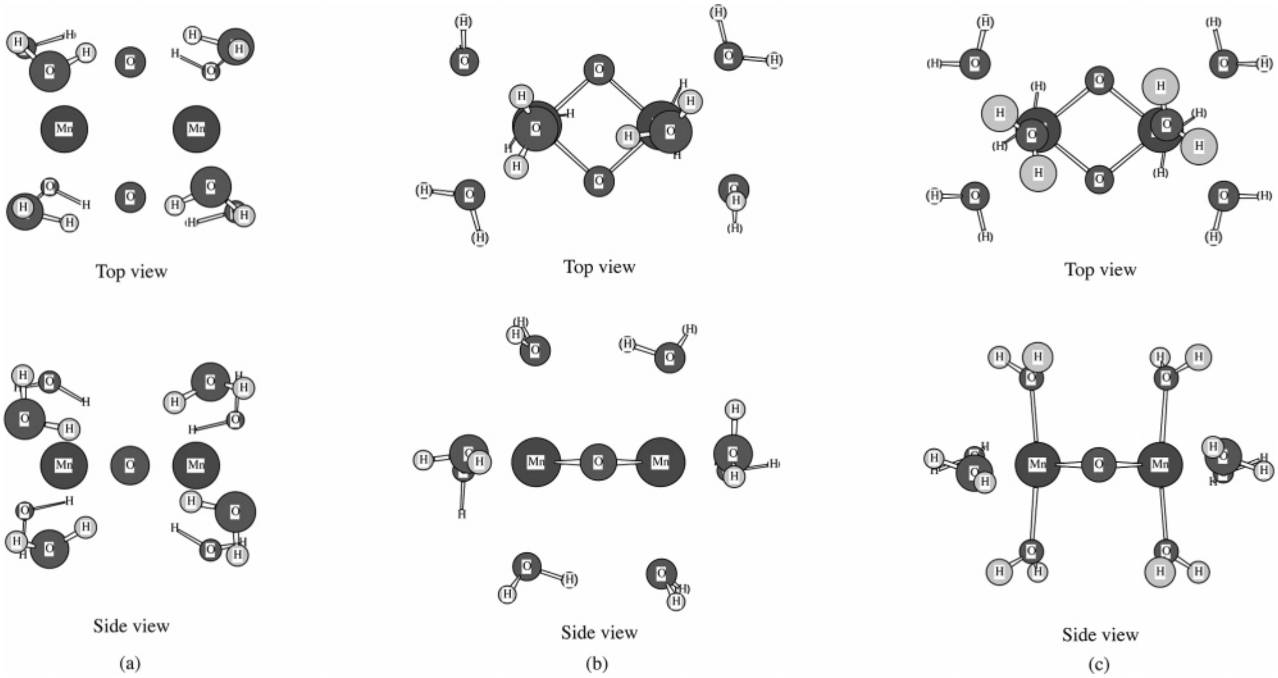

Figure 4. Optimized structures of iso-valence complexes in the lowest-spin configuration: (a) $Mn_2O_2(H_2O)_8$ (**1**), (b) $[Mn_2O_2(H_2O)_8]^{2+}$ (**2**), and (c) $[Mn_2O_2(H_2O)_8]^{4+}$ (**3**).

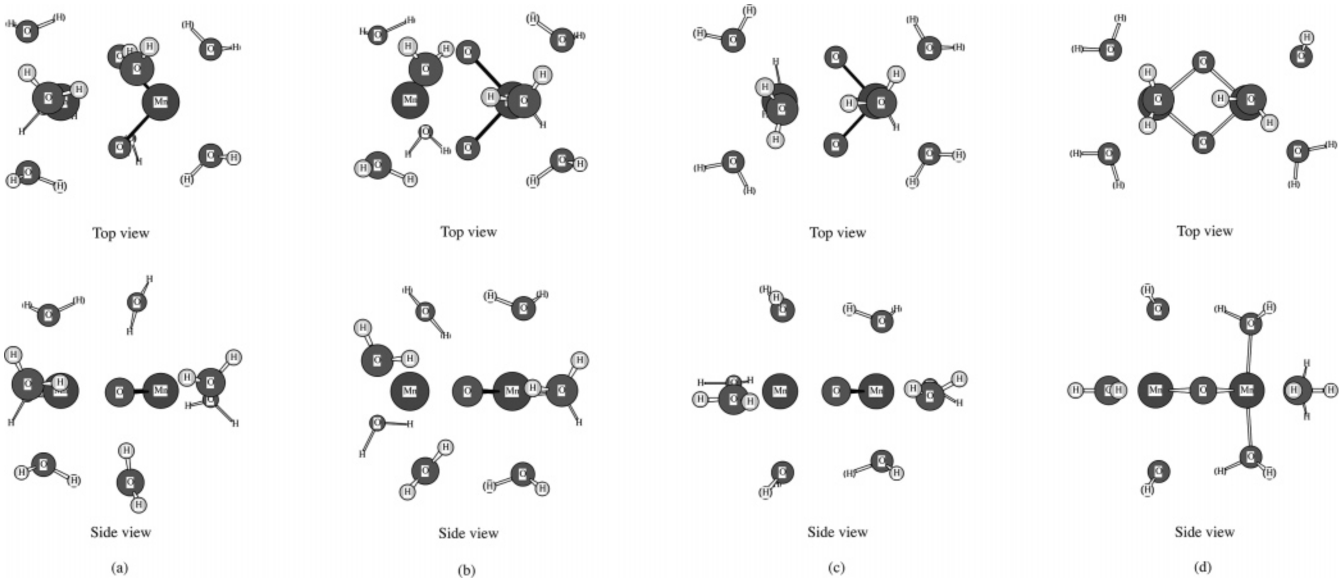

Figure 5. Optimized structures of mixed-valence complexes in the lowest-spin configuration: (a) $[Mn_2O_2(H_2O)_8]^+$ (**4a**), (b) $[Mn_2O_2(H_2O)_8]^+$ (**4b**), (c) $[Mn_2O_2(H_2O)_8]^{2+}$ (**5**), and (d) $[Mn_2O_2(H_2O)_8]^{3+}$ (**6**).

configurations are nearly pure spin states and the lowest-spin configurations are the broken-symmetry states, which respectively include the five (**1**), four (**2**, **4a**, and **4b**), and three (**3**, **5**, and **6**) pairs of singlet-coupled biradical electrons.

The relative energies indicate that the lowest-spin couplings are energetically more stable than the highest-spin couplings. The energy differences between both spin configurations for the complexes with the Mn(II) oxidation state are remarkably smaller than those for the complexes without the Mn(II) oxidation state: 0.2 kcal/mol for **1** with Mn(II)−Mn(II), 0.6 kcal/mol for **4a** and **4b** with Mn(II)−Mn(III), and 0.1 kcal/mol for **5** with Mn(II)−Mn(IV) < 7.1 kcal/mol for **2** with Mn(III)−Mn(III), 2.8 kcal/mol for **3** with Mn(IV)−Mn(IV), and 5.7 kcal/mol for **6** with Mn(III)−Mn(IV), suggesting that the magnetic interactions are weak in the Mn(II)-contained complexes.

V. Stable Geometry of Model Complex

Figures 4 and 5, respectively, show the optimized structures of iso- and mixed-valence complexes in the lowest-spin configurations as Figures 4a for **1**, 4b for **2**, and 4c for **3** and as Figures 5a for **4a**, 5b for **4b**, 5c for **5**, and 5d for **6**. We note that the optimized structures of complexes in the highest-spin configurations are not given in these figures because they have locations and orientations similar to those of H_2O molecules at the lowest-spin configurations. The coordinated H_2O ligands occupy the different positions in **1**, **4**, and the others, respectively, and the hydrogen bonds are found in the optimized geometries except in **3**. In this section, the numbering of the H and O atoms from 5−12 corresponds to the numbering of the H_2O molecules indicated in Figure 3.

The H_2O ligands of **1** move from the octahedral positions by rotating around the Mn−Mn axis, and one of the H atoms in each of the H_2O molecules faces the μ-oxo ions to form hydrogen bonds with the O−H distances of R(O3−H5), R(O4−H6), R(O4−H7), and R(O3−H8) = 1.694−1.697 Å and R(O3−H9), R(O4−H10), R(O3−H11), and R(O4−H12) = 1.665−1.668 Å (lowest-spin configuration). Although the H_2O ligands of **2** and **3** occupy the octahedral positions, their orientations differ from each other. The axial H_2O ligands of **2** make the hydrogen bondings above and below the Mn_2O_2 core with O−H distances of R(O5−H7) = R(O8−H6) = 1.982 Å (lowest-spin configuration), whereas the H_2O ligands of **3** seem to have no hydrogen bondings between μ-oxo ions and H_2O molecules or between H_2O molecules.

It is characteristic for **4a** and **4b** that two types of hydrogen bonds are observed although they have different positions of H_2O ligands. Two axial H_2O molecules are located at the octahedral positions of Mn1 (**4a**) or Mn2 (**4b**) corresponding to Mn(II) or Mn(III), whereas the other axial H_2O molecules seem to coordinate to μ-oxo ions rather than to Mn ions. The hydrogen bonds are formed between axial H_2O ligands above and below the Mn_2O_2 core, and the axial H_2O ligands shifted from the octahedral positions also make hydrogen bonds with μ-oxo ions. The hydrogen bond O−H distances are obtained as follows: R(O3−H7) = 1.709 Å and R(O4−H8) = 1.700 Å between the μ-oxo ion and the H_2O molecule and R(O7−H5) = 1.763 Å and R(O8−H6) = 1.731 Å between H_2O molecules (lowest-spin configuration of **4a**); R(O3−H5) = 1.643 Å and R(O4−H6) = 1.642 Å between the μ-oxo ion and H_2O molecule and R(O5−H7) = 1.972 Å and R(O6−H8) = 1.971 Å between H_2O molecules (lowest-spin configuration of **4b**). We note that although several energy minima of **4**, in which the H_2O ligands are fully placed at the octahedral positions and the hydrogen bonds are formed between axial H_2O molecules similar to **2**, were found, their structures were higher in energy than **4a** and **4b** by more than ∼7 kcal/mol as described in section IV. The octahedral geometries of H_2O ligands are favorable to **5** and **6**, and hydrogen bonds are found between axial H_2O molecules as seen in **2**. The hydrogen bond O−H distances are obtained as follows: R(O5−H7) = R(O6−H8) = 1.924 Å (lowest-spin configuration of **5**); R(O5−H7) = 1.857 Å and R(O6−H8) = 1.855 Å (lowest-spin configuration of **6**).

Although the axial H_2O ligands of **2** and **4**−**6** form hydrogen bonds with each other as mentioned above, the roles are different between **2** and **4**−**6** in the most stable coordinations. Two of the axial H_2O molecules coordinated to the same Mn ion play different and the same roles as the hydrogen donor or hydrogen acceptor in **2** and **4**−**6**, respectively. The axial H_2O ligands of **2**, **5**, and **6** at the octahedral positions have shorter Mn−OH_2 distances for the hydrogen donor than they do for the hydrogen accepter as Mn−OH_2 (donor) ≈ 2.25 Å < Mn−OH_2 (acceptor) ≈ 2.41 Å for **2**, Mn−OH_2 (donor) ≈ 2.01 Å < Mn−OH_2 (acceptor) ≈ 2.33 Å for **5**, and Mn−OH_2 (donor) ≈ 1.97 Å < Mn−OH_2 (acceptor) ≈ 2.36 Å for **6** (lowest-spin configuration), where the H_2O molecules of the hydrogen donor (acceptor) are coordinated to the higher (lower) oxidation site of the Mn−Mn center in the mixed-valence complexes **5** and **6**.

We compared the hydrogen bonds found in **1**, **2**, and **4**−**6**. The hydrogen bond lengths between the μ-oxo ion and the H_2O molecule are about 1.70 and 1.67 Å in **1**, about 1.70 Å in **4a**, and about 1.64 Å in **4b**, which are shorter, with the exception of **4a**, than the hydrogen-bond lengths between the H_2O molecules ranging from about 1.86−1.98 Å in **2**, **4b**, **5**, and **6**. These additional hydrogen bonds would be the reason why **4a** and **4b** have lower energies than the other energy minima of **4**. The hydrogen bonds between H_2O molecules are shorter in **4a** (∼1.73 and 1.76 Å) than they are in **2** (∼1.98 Å), **4b** (∼1.97 Å), **5** (∼1.92 Å), and **6** (∼1.86 Å).

With the exception of the complex including the Mn(II)−Mn(IV) core (**5**), the most-stable coordination positions of the H_2O molecules are different between the complexes. The Mn(II) ion (**1** and **4**) has some shifted H_2O ligands, and the complexes without the Mn(II) ion (**2**, **3**, and **6**) have eight octahedral H_2O ligands. Because all of the octahedral e_g orbitals, which indicate the antibonding nature between Mn ions and both H_2O ligands in the axial and equatorial directions, are singly occupied in the Mn(II) oxidation state, it is expected that the Mn(II)−OH_2 bindings become loose. It is thus likely that the H_2O ligands coordinated to the Mn(II) ion would move from the octahedral positions to the more stable positions, which enable them to make hydrogen bonds with μ-oxo ions.

Figure 6 shows the optimized interatomic distances and angles of iso- and mixed-valence complexes in the lowest-spin configuration as Figures 6a for Mn−Mn, 6b for O−O, 6c for Mn−O, 6d for Mn−OH_2 (axial), 6e for Mn−OH_2 (equatorial), 6f for Mn−O−Mn, and 6g for O−Mn−O. The optimized values of these parameters for the complexes in both of the highest- and lowest-spin configurations are given in Appendix A. In Figures 6a−6g, the oxidation states of the Mn1−Mn2 center in the mixed-valence complexes correspond to Mn(II)−Mn(III) for **4a** and **4b**, Mn(II)−Mn(IV) for **5**, and Mn(III)−Mn(IV) for **6**, respectively.

It is found from Figure 6a that the Mn−Mn separations seem to have no relation to the formal oxidation states of Mn ions as Mn(II)−Mn(II) in **1** > Mn(II)−Mn(III) in **4a** and **4b** > Mn(IV)−Mn(IV) in **3** and Mn(II)−Mn(IV) in **5** > Mn(III)−Mn(IV) in **6** > Mn(III)−Mn(III) in **2**, although the order of the Mn−Mn lengths may be expected simply from the electrostatic repulsion between the formal charges on Mn ions as Mn(II)−Mn(II) in **1** < Mn(II)−Mn(III) in **4a** and **4b** < Mn(II)−Mn(IV) in **5** < Mn(III)−Mn(III) in **2** < Mn(III)−Mn(IV) in **6** < Mn(IV)−Mn(IV) in **3**. The O−O and Mn−O distances shown in Figures 6b and 6c also vary depending on the oxidation states of complexes as O−O for the $Mn(II)_2O_2$ core in **1** > O−O for the $Mn(II)Mn(III)O_2$ core in **4a** and **4b** > O−O for the $Mn(II)Mn(IV)O_2$ core in **5** > O−O for the $Mn(III)_2O_2$ core in **2** > O−O for the $Mn(III)Mn(IV)O_2$ core in **6** > O−O for the $Mn(IV)_2O_2$ core in **3** and as Mn(II)−O in **1**, **4a**, **4b**, and **5** > Mn(III)−O in **2**, **4a**, **4b**, and **6** and Mn(IV)−O in **3**, **5**, and **6**. The Mn(II) centers have the Mn−O lengths near 2.1 Å, whereas the Mn(III) and Mn(IV) centers have the Mn−O lengths around 1.7−1.8 Å, suggesting that more repulsive interactions would act between Mn(II) and μ-oxo ions than they would between Mn(III) or Mn(IV) and μ-oxo ions. The coordination distances of the octahedral H_2O ligands to the Mn ions given in Figures 6d and 6e indicate the features that Mn(II)−OH_2 in **4a** and **5** and Mn(III)−OH_2 in **2**, **4b**, and **6** > Mn(IV)−OH_2 in **3**, **5**, and **6** for the axial positions (Figure 6d) and Mn(II)−OH_2 in **4a**, **4b**, and **5** > Mn(III)−OH_2 in **2**, **4a**, **4b**, and **6** and Mn(IV)−OH_2 in **3**, **5**, and **6** for the equatorial positions (Figure 6e), although the differences are smaller for the equatorial ligands, especially in **4b** and **5**, than they are for the axial ligands.

Figure 6f indicates that the higher the Mn ions are oxidized, the larger the Mn−O−Mn angles become for the iso-valence complexes, and the Mn−O−Mn angles for the mixed-valence complexes lie between the values in the corresponding iso-valence states, which include one of the component Mn ions in the mixed-valence states as follows: Mn(II)−O−Mn(II) in **1**

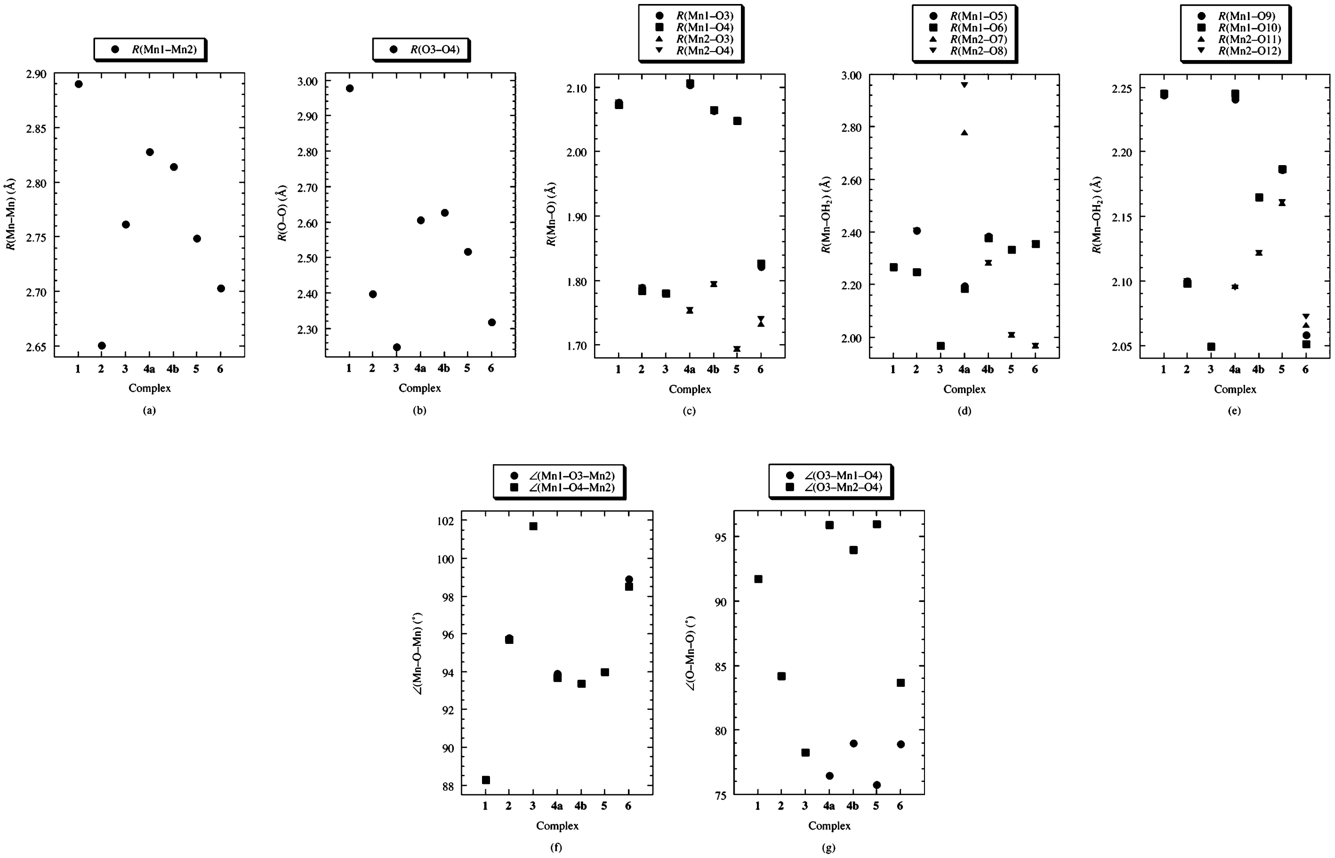

Figure 6. Optimized interatomic distances and angles of iso- and mixed-valence complexes $[Mn_2O_2(H_2O)_8]^{q+}$ in the lowest-spin configuration: (a) Mn−Mn, (b) O−O, (c) Mn−O, (d) $Mn-OH_2$ (axial), (e) $Mn-OH_2$ (equatorial), (f) Mn−O−Mn, and (g) O−Mn−O.

TABLE 2: Experimental and Theoretical Structures of the Mn_2O_2 Core in Iso-Valence Mn_2O_2 Complexes

oxidation state	Mn−Mn[a]	O−O[a]	Mn−O[a]	O−Mn−O[b]	ref
		experiment			
Mn(III)−Mn(III)	2.674−2.686		1.830−1.842	86.1−86.7	30
	2.674−2.699	2.500−2.526	1.830−1.848		34
Mn(IV)−Mn(IV)	2.672−2.748		1.774−1.811	78.5−85.0	30
	2.568−2.780	2.246−2.538	1.774−1.834		34
		calculation			
Mn(II)−Mn(II)	2.890	2.978	2.073−2.076	91.7	this work
Mn(III)−Mn(III)	2.651	2.397	1.784, 1.790	84.2	this work
	2.716		1.840	84.8	30
	2.791	2.433	1.852		34
	2.690	2.465	1.797, 1.851		37
Mn(IV)−Mn(IV)	2.762	2.249	1.781	78.3	this work
	2.866		1.842	77.9	30
	2.902	2.283	1.846		34
	2.834	2.272	1.789, 1.842		37

[a] Interatomic distances are given in angströms. [b] Interatomic angles are given in degrees.

< Mn(II)−O−Mn(III) in **4a** and **4b** and Mn(II)−O−Mn(IV) in **5** < Mn(III)−O−Mn(III) in **2** < Mn(III)−O−Mn(IV) in **6** < Mn(IV)−O−Mn(IV) in **3**. It is found from Figure 6g that the O−Mn−O angle has the tendency to become more acute for the higher-oxidized Mn ion compared among the iso-valence complexes and has the tendency to become more obtuse for the higher-oxidized Mn ion compared within the mixed-valence complex as follows: O−Mn(II)−O in **1** > O−Mn(III)−O in **2** > O−Mn(IV)−O in **3** (iso-valence complexes); O−Mn(II)−O < O−Mn(III)−O in **4a** and **4b**, O−Mn(II)−O < O−Mn(IV)−O in **5**, and O−Mn(III)−O < O−Mn(IV)−O in **6** (mixed-valence complexes).

These changes in molecular geometry, depending on the oxidation state of complexes described above, would be caused by the changes in electron occupation of the Mn−O and $Mn-OH_2$ antibonding orbitals with the oxidation of the Mn−Mn center.

Some of the geometrical parameters of di-μ-oxo-bridged Mn_2O_2 complexes with various ligands (mainly N-donor) observed by experiments and those of $[Mn_2O_2(NH_3)_8]^{q+}$ and $[Mn_2O_2(NH_3)_6(H_2O)_2]^{q+}$ calculated by the broken-symmetry DFT method within the spatial symmetry framework have been summarized in refs 30, 34, and 37, and the available data for the Mn_2O_2 core in the iso- and mixed-valence oxidation states are listed in Tables 2 and 3, respectively, together with the results of $[Mn_2O_2(H_2O)_8]^{q+}$ determined in this work. In these Tables, the ranges of the experimental values and the theoretical

TABLE 3: Experimental and Theoretical Structures of the Mn_2O_2 Core in Mixed-Valence Mn_2O_2 Complexes

oxidation state	Mn−Mn[a]	O−O[a]	Mn−O[a,c]	Mn−O[a,d]	O−Mn−O[b,c]	O−Mn−O[b,d]	ref
			experiment				
Mn(III)−Mn(IV)	2.643−2.741		1.833−1.862	1.774−1.793	80.6−82.5	84.6−86.8	30
	2.553−2.741	2.373−2.525	1.81−1.89	1.77−1.81			34
			calculation				
Mn(II)−Mn(III)	2.828	2.606	2.103, 2.106	1.754, 1.755	76.5	95.9	this work
	2.814	2.628	2.063, 2.065	1.795	79.0	94.0	this work
	2.833	2.635	2.063	1.813			34
Mn(II)−Mn(IV)	2.749	2.517	2.048	1.694	75.8	96.0	this work
Mn(III)−Mn(IV)	2.703	2.318	1.822, 1.827	1.733, 1.740	78.9	83.7	this work
	2.783		1.873	1.800	79.5	85.2	30
	2.845	2.358	1.921	1.777			34
	2.761	2.353	1.773−1.864				37

[a] Interatomic distances are given in angströms. [b] Interatomic angles are given in degrees. [c] Geometrical parameters for the lower oxidation state of Mn ion are shown. [d] Geometrical parameters for the higher oxidation state of Mn ion are shown.

values optimized for the most-stable broken-symmetry states are given concerning the Mn−Mn, O−O, Mn−O, and O−Mn−O parameters.

Our results are comparable with the reported experimental and theoretical results, and the changes in the Mn_2O_2 structure as Mn(III)−Mn(III) < Mn(III)−Mn(IV) < Mn(IV)−Mn(IV), O−O for the Mn(III)$_2$O$_2$ core > O−O for the Mn(III)Mn(IV)-O$_2$ core > O−O for the Mn(IV)$_2$O$_2$ core, Mn(III)−O ≈ Mn(IV)−O and O−Mn(III)−O > O−Mn(IV)−O for the Mn(III)$_2$O$_2$ and Mn(IV)$_2$O$_2$ cores, and Mn(III)−O > Mn(IV)−O and O−Mn(III)−O < O−Mn(IV)−O for the Mn(III)Mn(IV)-O$_2$ core are consistent among the calculations in this work and in the other work. Although the experimental data are lacking for the complexes containing Mn(II)−Mn(II), Mn(II)−Mn(III), and Mn(II)−Mn(IV) centers, the theoretical geometries of Mn(II)−Mn(III) complex in the present study correspond to those in the early study.

From comparison of the optimized geometries in the Mn(III)−Mn(III), Mn(IV)−Mn(IV), and Mn(III)−Mn(IV) oxidation states between $[Mn_2O_2(H_2O)_8]^{q+}$ in this work and $[Mn_2O_2(NH_3)_8]^{q+}$ shown in ref 30, it is found that the Mn−O distances in the Mn_2O_2 core become shorter in complexes with H_2O ligands than in complexes with NH_3 ligands by about 0.05−0.07 Å, whereas the O−Mn−O angles are almost the same in both types of complex, and in consequence the Mn−Mn separations are shorter in the former than they are in the latter. The distances between Mn ions and NH_3 ligands in $[Mn_2O_2(NH_3)_8]^{q+}$ were reported in ref 30 as follows for the axial and equatorial positions: 2.504 and 2.231 Å in the Mn(III)−Mn(III) complex, 2.137 and 2.215 Å in the Mn(IV)−Mn(IV) complex, 2.459 and 2.210 Å for Mn(III); and 2.117 and 2.227 Å for Mn(IV) in the Mn(III)−Mn(IV) complex. It was also pointed out in ref 30 that the axial Mn−NH_3 length at the Mn(III) site in the mixed-valence system (2.459 Å) is significantly shorter than that in the iso-valence system (2.504 Å), whereas the structural characteristics of the Mn(IV) site in the mixed-valence system are almost identical to those in the iso-valence system, suggesting that an extra electron in the mixed-valence complex is not completely localized in the d_{z^2} orbital on the Mn(III) center and, however, its electron density is not transferred into the d_{z^2} orbital on the Mn(IV) center (The C_{2v} restriction was applied to the spatial symmetry of model complexes in ref 30). In the case of $[Mn_2O_2(H_2O)_8]^{q+}$, the H_2O ligands have the following distances from Mn ions: 2.250 and 2.251 Å (axial hydrogen donor), 2.405 and 2.406 Å (axial hydrogen acceptor), and 2.098 and 2.100 Å (equatorial) in the Mn(III)−Mn(III) complex; 1.968 Å (axial) and 2.049 Å (equatorial) in the Mn(IV)−Mn(IV) complex; 2.356 and 2.357 Å (axial hydrogen acceptor) and 2.051 and 2.058 Å (equatorial) for Mn(III) and 1.969 (axial hydrogen donor) and 2.066 and 2.072 Å (equatorial) for Mn(IV) in the Mn(III)−Mn(IV) complex, as shown in Appendix A (Table A3). Although the distances between Mn ions and axial or equatorial H_2O ligands in these oxidation states also become shorter in $[Mn_2O_2(H_2O)_8]^{q+}$ than in $[Mn_2O_2(NH_3)_8]^{q+}$ by about 0.1−0.15 Å, they indicate similar geometrical characteristics to those of $[Mn_2O_2(NH_3)_8]^{q+}$ described above for the axial H_2O ligands of the hydrogen acceptor at the Mn(III) site and the H_2O ligands at the Mn(IV) site.

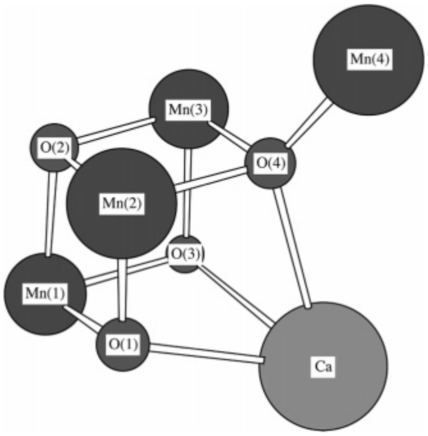

Figure 7. X-ray structure of the cubanelike Mn_3CaO_4−Mn cluster in the OEC (pdb code: 1S5L)[19] and numbering of atoms.

TABLE 4: X-ray Interatomic Distances for Mn−Mn, O−O, and Mn−O Pairs of the Cubanelike Mn_3CaO_4−Mn Cluster in the OEC (pdb code: 1S5L)[19]

Mn−Mn (angströms)		O−O (angströms)		Mn−O (angströms)	
Mn(1)−Mn(2)	2.648	O(1)−O(2)	2.500	Mn(1)−O(1)	1.872
Mn(1)−Mn(3)	2.669	O(1)−O(3)	2.694	Mn(1)−O(2)	1.824
Mn(1)−Mn(4)	5.127	O(1)−O(4)	2.661	Mn(1)−O(3)	1.863
Mn(2)−Mn(3)	2.718	O(2)−O(3)	2.487	Mn(2)−O(1)	1.770
Mn(2)−Mn(4)	3.249	O(2)−O(4)	2.563	Mn(2)−O(2)	1.821
Mn(3)−Mn(4)	3.255	O(3)−O(4)	2.696	Mn(2)−O(4)	1.938
				Mn(3)−O(2)	1.802
				Mn(3)−O(3)	1.809
				Mn(3)−O(4)	1.912
				Mn(4)−O(4)	1.866

Here, we compare the theoretical and experimental Mn−Mn, O−O, and Mn−O distances among our model complexes and the cubanelike cluster in the OEC. The X-ray structure[19] and X-ray distances are shown in Figure 7 and in Table 4, respectively. It is noted that because the resolution of the X-ray crystal structure is 3.5 Å and the model complexes are Mn−

TABLE 5: Mulliken Charge and Spin Densities on Atoms in the Mn_2O_2 Core of Iso- and Mixed-Valence Complexes $[Mn_2O_2(H_2O)_8]^{q+}$

		charge density				spin density			
complex	*S*	Mn1	Mn2	O3	O4	Mn1	Mn2	O3	O4
1	10/2	1.297	1.297	−1.109	−1.108	4.756	4.756	0.138	0.137
	0/2	1.294	1.294	−1.111	−1.112	4.754	−4.754	−0.000	0.001
2	8/2	1.537	1.536	−0.908	−0.908	3.866	3.865	0.070	0.070
	0/2	1.521	1.521	−0.889	−0.889	3.814	−3.814	0.003	−0.003
3	6/2	1.725	1.725	−0.665	−0.665	3.024	3.024	−0.046	−0.046
	0/2	1.718	1.718	−0.660	−0.660	2.871	−2.871	−0.000	0.000
4a	9/2	1.372	1.410	−1.008	−1.009	4.791	3.785	0.147	0.147
	1/2	1.375	1.408	−1.010	−1.011	4.762	−3.800	−0.018	−0.018
4b	9/2	1.366	1.480	−1.043	−1.043	4.773	3.822	0.117	0.118
	1/2	1.364	1.478	−1.044	−1.043	4.746	−3.849	0.044	0.044
5	8/2	1.408	1.566	−0.891	−0.891	4.772	2.662	0.250	0.250
	2/2	1.414	1.565	−0.895	−0.895	4.740	−2.615	−0.114	−0.114
6	7/2	1.604	1.683	−0.759	−0.789	3.906	2.938	0.050	0.044
	1/2	1.599	1.664	−0.742	−0.772	3.939	−2.676	−0.201	−0.171

Mn binuclear complexes the comparisons of theoretical and experimental results are therefore qualitative.

The cubanelike faces of the Mn cluster in the OEC are composed of Mn−Mn pairs of Mn(1)−Mn(2), Mn(1)−Mn(3), and Mn(2)−Mn(3) as seen in Figure 7, and these pairs have distances of 2.648, 2.669, and 2.718 Å for the Mn−Mn separation, respectively. The optimized separations for Mn(III)−Mn(III), Mn(IV)−Mn(IV), Mn(II)−Mn(IV), and Mn(III)−Mn(IV) in **2**, **3**, **5**, and **6** are respectively comparable with the experimental values as 2.651, 2.762, 2.749, and 2.703 Å, whereas the theoretical Mn(II)−Mn(II) and Mn(II)−Mn(III) distances of 2.890, 2.828, and 2.814 Å in **1**, **4a**, and **4b** are much longer than the experimental distances.

Concerning the O−O distances of di-μ-oxo bridges within cubanelike faces, the experimental values were reported as O(1)−O(2) = 2.500 Å, O(2)−O(3) = 2.487 Å, and O(2)−O(4) = 2.563 Å. However, the O(1), O(3), and O(4) ions bond with the Ca ion, and the O(4) ion bonds with the outer Mn(4) ion. It is thus considered that the experimental O−O lengths are strongly affected by these ions. Although the theoretical values for iso-valence complexes **2** and **3** are shorter than the experimental values like O−O in **2** with the Mn(III)−Mn(III) center = 2.397 Å and O−O in **3** with the Mn(IV)−Mn(IV) center = 2.249 Å, among interatomic separations, the tendency for the Mn−Mn bond to be longer than the O−O bond is consistent between the experiments and calculations. The optimized value for iso-valence complex **1** with the Mn(II)−Mn(II) center indicates that the theoretical O−O length of 2.978 Å is much longer than the experimental lengths and is also longer than the theoretical Mn(II)−Mn(II) length. The theoretical values of O−O separations are 2.606, 2.628, 2.517, and 2.318 Å, respectively, for mixed-valence complexes **4a**, **4b**, **5**, and **6**. The distance for **5** in the Mn(II)−Mn(IV) oxidation state shows similarity to the experimental values, and the distances for **4a** and **4b** in the Mn(II)−Mn(III) oxidation state and for **6** in the Mn(III)−Mn(IV) oxidation state seem to be longer and shorter than the experimental values, respectively.

The experimental Mn−O lengths range from 1.770 to 1.938 Å. The Mn(2)−O(4) and Mn(3)−O(4) give longer separations of 1.938 and 1.912 Å, respectively, in which the O(4) ion interacts with the Mn(4) and Ca ions. The Mn(1)−O(1) and Mn(1)−O(3) also give longer separations of 1.872 and 1.863 Å, respectively, in which the O(1) and O(3) ions interact with the Ca ion. The Mn(1)−O(2), Mn(2)−O(1), Mn(2)−O(2), Mn(3)−O(2), and Mn(3)−O(3) give shorter separations of 1.824, 1.770, 1.821, 1.802, and 1.809 Å, respectively. The theoretical Mn−O distances obtained are 1.784 and 1.790 Å for **2**, 1.781 Å for **3**, and 2.073−2.076 Å for **1**, indicating that the results for Mn(III)−Mn(III) and Mn(IV)−Mn(IV) complexes show similarity to the shorter experimental values. The optimized Mn−O distances of 2.063−2.106 Å for Mn(II)−O and 1.754−1.795 Å for Mn(III)−O in **4a** and **4b**, 2.048 Å for Mn(II)−O and 1.694 Å for Mn(IV)−O in **5**, and 1.822 and 1.827 Å for Mn(III)−O and 1.733 and 1.740 Å for Mn(IV)−O in **6** suggest that the Mn(II)−O in **4a**, **4b**, and **5** and the Mn(IV)−O in **5** would be too long and too short in comparison with the experimental distances, respectively, whereas the calculated Mn(III)−O and Mn(IV)−O separations in **6** may be comparable to the experimental values of the Mn(1)−O(1)−Mn(2)−O(2) or the Mn(1)−O(2)−Mn(3)−O(3) cubanelike faces.

Judging from the comparison of interatomic distances in the experiments and calculations described above, it may be possible to suggest that the cubanelike Mn_3CaO_4 cluster in the OEC contains the low-spin-coupled Mn(III)−Mn(III), Mn(IV)−Mn(IV), or Mn(III)−Mn(IV) pairs, and the Mn(II) oxidation state is not included.

VI. Mulliken Population Analysis of Model Complex

We summarize the charge and spin densities on atoms in the Mn_2O_2 core of the iso- and mixed-valence complexes in Table 5. Tables 6 and 7 also show the gross orbital populations in the Mn 3d orbitals of the iso- and mixed-valence complexes in the lowest-spin configuration, respectively. As described in the next section, the octahedral e_g orbitals of the Mn−Mn center in the axial direction are assigned for each complex to be $d_{y^2-z^2}$ for **1**, $d_{x^2-z^2}$ for **2**, d_{z^2} for **3**, $d_{x^2-z^2}$ on Mn(II) and $d_{y^2-z^2}$ on Mn(III) for **4**, d_{z^2} on Mn(II) and Mn(IV) for **5**, and $d_{y^2-z^2}$ on Mn(III) and d_{z^2} on Mn(IV) for **6**.

The charge densities on the Mn and μ-oxo ions in the lowest-spin configuration are respectively obtained as follows: 1.29 for Mn(II) and −1.11 for O in **1**; 1.52 for Mn(III) and −0.89 for O in **2**; 1.72 for Mn(IV) and −0.66 for O in **3**; 1.38 for Mn(II), 1.41 for Mn(III), and −1.01 for O in **4a**; 1.36 for Mn(II), 1.48 for Mn(III), and −1.04 for O in **4b**; 1.41 for Mn(II), 1.57 for Mn(IV), and −0.90 for O in **5**; 1.60 for Mn(III), 1.66 for Mn(IV), and −0.74 and −0.78 for O in **6**, which are much smaller than the formal charges of 2+, 3+, 4+, and 2− for the Mn(II), Mn(III), Mn(IV), and μ-oxo ions, respectively, indicating that the significant charge delocalization (electron transfer) occurs mainly from di-μ-oxo ions to Mn ions. The differences in atomic charge at the Mn(II), Mn(III), Mn(IV), and μ-oxo sites are not as remarkable as expected from their formal charges, and it may be suggested that the influences of the

TABLE 6: Mulliken Gross Orbital Populations in Mn 3d Orbitals of Iso-Valence Complexes $[Mn_2O_2(H_2O)_8]^{q+}$ in the Lowest-Spin Configuration

		Mn1					Mn2			
complex	3d orbital[a]	total	alpha	beta	spin	3d orbital[a]	total	alpha	beta	spin
1	d_{xz}	1.064	1.003	0.061	0.942	d_{xz}	1.064	0.061	1.003	−0.943
	d_{yz}	1.033	1.001	0.032	0.968	d_{yz}	1.033	0.032	1.001	−0.968
	d_{x^2}	1.029	0.987	0.042	0.945	d_{x^2}	1.030	0.042	0.987	−0.945
	d_{xy}	1.118	1.001	0.117	0.884	d_{xy}	1.118	0.117	1.001	−0.884
	$d_{y^2-z^2}$	1.032	0.995	0.037	0.959	$d_{y^2-z^2}$	1.032	0.037	0.995	−0.959
2	d_{xz}	1.100	0.996	0.104	0.892	d_{xz}	1.100	0.104	0.996	−0.892
	d_{yz}	1.100	1.001	0.099	0.902	d_{yz}	1.100	0.099	1.001	−0.902
	d_{y^2}	1.111	0.994	0.116	0.879	d_{y^2}	1.111	0.116	0.995	−0.879
	d_{xy}	0.728	0.473	0.255	0.219	d_{xy}	0.728	0.255	0.473	−0.219
	$d_{x^2-z^2}$	1.101	0.988	0.113	0.874	$d_{x^2-z^2}$	1.101	0.113	0.988	−0.874
3	d_{xz}	1.160	0.989	0.170	0.819	d_{xz}	1.160	0.170	0.989	−0.819
	d_{yz}	1.194	1.002	0.192	0.810	d_{yz}	1.194	0.192	1.002	−0.810
	$d_{x^2-y^2}$	0.987	0.818	0.170	0.648	$d_{x^2-y^2}$	0.987	0.170	0.818	−0.648
	d_{xy}	0.865	0.537	0.327	0.210	d_{xy}	0.865	0.327	0.537	−0.210
	d_{z^2}	0.782	0.569	0.212	0.357	d_{z^2}	0.782	0.212	0.569	−0.357

[a] First three and last two orbitals correspond to octahedral t_{2g} and e_g orbitals, respectively, for each complex.

TABLE 7: Mulliken Gross Orbital Populations in Mn 3d Orbitals of Mixed-Valence Complexes $[Mn_2O_2(H_2O)_8]^{q+}$ in the Lowest-Spin Configuration

		Mn1					Mn2			
complex	3d orbital[a]	total	alpha	beta	spin	3d orbital[a]	total	alpha	beta	spin
4a	d_{xz}	1.024	0.997	0.027	0.970	d_{xz}	1.144	0.142	1.002	−0.860
	d_{yz}	1.028	0.999	0.028	0.971	d_{yz}	1.113	0.112	1.001	−0.888
	d_{y^2}	1.033	0.996	0.037	0.960	d_{x^2}	1.065	0.110	0.955	−0.844
	d_{xy}	1.100	1.002	0.098	0.904	d_{xy}	0.763	0.281	0.482	−0.201
	$d_{x^2-z^2}$	1.064	0.997	0.067	0.931	$d_{y^2-z^2}$	1.109	0.113	0.996	−0.882
4b	d_{xz}	1.044	0.998	0.046	0.952	d_{xz}	1.101	0.101	1.000	−0.899
	d_{yz}	1.030	1.000	0.030	0.971	d_{yz}	1.088	0.087	1.001	−0.914
	d_{y^2}	1.041	0.997	0.044	0.952	d_{x^2}	1.112	0.123	0.989	−0.865
	d_{xy}	1.118	1.002	0.116	0.886	d_{xy}	0.733	0.262	0.471	−0.210
	$d_{x^2-z^2}$	1.037	0.990	0.047	0.942	$d_{y^2-z^2}$	1.097	0.098	1.000	−0.902
5	d_{xz}	1.024	0.993	0.030	0.963	d_{xz}	1.269	0.269	1.000	−0.732
	d_{yz}	1.033	1.000	0.033	0.966	d_{yz}	1.220	0.218	1.001	−0.783
	$d_{x^2-y^2}$	1.035	0.995	0.040	0.954	$d_{x^2-y^2}$	1.097	0.185	0.912	−0.728
	d_{xy}	1.120	1.004	0.117	0.887	d_{xy}	0.833	0.343	0.491	−0.148
	d_{z^2}	1.037	0.991	0.047	0.944	d_{z^2}	0.710	0.256	0.454	−0.198
6	d_{xz}	1.076	0.994	0.082	0.913	d_{xz}	1.198	0.199	1.000	−0.801
	d_{yz}	1.089	0.999	0.090	0.910	d_{yz}	1.209	0.207	1.001	−0.794
	d_{x^2}	1.077	0.990	0.087	0.904	$d_{x^2-y^2}$	1.032	0.209	0.823	−0.614
	d_{xy}	0.753	0.510	0.243	0.266	d_{xy}	0.817	0.334	0.483	−0.148
	$d_{y^2-z^2}$	1.079	0.992	0.087	0.905	d_{z^2}	0.791	0.247	0.544	−0.296

[a] The first three and last two orbitals correspond to octahedral t_{2g} and e_g orbitals, respectively, for each complex.

electrostatic interactions among the Mn and μ-oxo ions in the different oxidation states on the Mn_2O_2 geometries would be rather small. The spin densities are mainly localized on the Mn ions as ±4.75 for Mn(II) in **1**, ±3.81 for Mn(III) in **2**, ±2.87 for Mn(IV) in **3**, 4.76 for Mn(II) and −3.80 for Mn(III) in **4a**, 4.75 for Mn(II) and −3.85 for Mn(III) in **4b**, 4.74 for Mn(II) and −2.62 for Mn(IV) in **5**, and 3.94 for Mn(III) and −2.68 for Mn(IV) in **6** (lowest-spin configurations), and the μ-oxo bridges have almost zero spin densities in the lowest-spin configurations with the exception of the mixed-valence complexes **5** and **6** including the Mn(IV) ions, whereas the small spin delocaliztion on the μ-oxo ions appears in the highest-spin configurations.

The charge densities on H_2O ligands in the lowest-spin configurations, which are not listed in Table 5, are distributed as follows: −0.04 and −0.05 for **1**; 0.03 and 0.09 (axial) and 0.12 (equatoriaal) for **2**; 0.26 (axial) and 0.22 (equatorial) for **3**; 0.01 and 0.00 (axial to Mn1), −0.02 (between Mn2 and μ-oxo), 0.04 (equatorial to Mn1), and 0.09 (equatorial to Mn2) for **4a**; −0.02 (between Mn1 and μ-oxo), 0.02 (axial to Mn2), 0.05 (equatorial to Mn1), and 0.08 (equatorial to Mn2) for **4b**; 0.10 (axial to Mn1), 0.12 (axial to Mn2), 0.08 (equatorial to Mn1), and 0.11 (equatorial to Mn2) for **5**; 0.13 (axial to Mn1), 0.17 (axial to Mn2), 0.15 and 0.16 (equatorial to Mn1), and 0.17 and 0.18 (equatorial to Mn2) for **6**. Relatively larger positive charges are found only for **3** with the Mn(IV)−Mn(IV) oxidation state, and it is thus likely that the axial H_2O molecules on each Mn ion in **3** are apart from each other without hydrogen bonds as shown in Figure 4c.

The electron populations for majority-spin components of oxidized Mn(III) and Mn(IV) ions indicate that the octahedral t_{2g} orbitals are always fully occupied with the populations near 1.0, and the oxidized electrons are removed from the octahedral e_g orbitals in which the primary and secondary oxidations from Mn(II) to Mn(III) and from Mn(III) to Mn(IV) occur in the equatorial (d_{xy}) and axial (d_{z^2}) orbitals, respectively. Concerning the Mn(IV) oxidation state, the $d_{x^2-y^2}$ populations of **3** and **6** indicate slightly lower values of about 0.82 for majority spin because of the mixing with the d_{z^2} orbital at the same Mn site. The nonzero populations for minority-spin components, in contrast to the formal oxidation states with zero populations, would be the contributions of the partial electron transfer of

TABLE 8: Mn-Based Natural Orbitals of Iso-Valence Complexes $[Mn_2O_2(H_2O)_8]^{q+}$ in the Lowest-Spin Configuration

natural orbital	**1**			**2**			**3**		
	n^a	Mn1	Mn2	n^a	Mn1	Mn2	n^a	Mn1	Mn2
LUMO+3							0.008^b	$+d_{z^2}$	$-d_{z^2}$
LUMO+2							0.011^b	$+d_{z^2}$	$+d_{z^2}$
LUMO+1				0.023^b	$+d_{xy}$	$-d_{xy}$	0.019^b	$+d_{xy}$	$-d_{xy}$
LUMO				0.038^b	$+d_{xy}$	$+d_{xy}$	0.036^b	$+d_{xy}$	$+d_{xy}$
SOMO+5	0.900^c	$+d_{x^2}$	$-d_{x^2}$						
SOMO+4	0.932^b	$+d_{xy}$	$-d_{xy}$	0.792^c	$+d_{xz}$	$+d_{xz}$			
SOMO+3	0.974^c	$+d_{xz}$	$+d_{xz}$	0.813^b	$+d_{x^2-z^2}$	$-d_{x^2-z^2}$	0.761^c	$+d_{yz}$	$-d_{yz}$
SOMO+2	0.993^b	$+d_{y^2-z^2}$	$+d_{y^2-z^2}$	0.858^c	$+d_{yz}$	$-d_{yz}$	0.761^c	$+d_{xz}$	$+d_{xz}$
SOMO+1	0.998^c	$+d_{yz}$	$+d_{yz}$	0.861^c	$+d_{y^2}$	$+d_{y^2}$	0.867^c	$+d_{x^2-y^2}$	$+d_{x^2-y^2}$
SOMO−1	1.002^c	$+d_{yz}$	$-d_{yz}$	1.139^c	$+d_{y^2}$	$-d_{y^2}$	1.133^c	$+d_{x^2-y^2}$	$-d_{x^2-y^2}$
SOMO−2	1.007^b	$+d_{y^2-z^2}$	$-d_{y^2-z^2}$	1.142^c	$+d_{yz}$	$+d_{yz}$	1.239^c	$+d_{xz}$	$-d_{xz}$
SOMO−3	1.026^c	$+d_{xz}$	$-d^{xz}$	1.187^b	$+d_{x^2-z^2}$	$+d_{x^2-z^2}$	1.239^c	$+d_{yz}$	$+d_{yz}$
SOMO−4	1.068^b	$+d_{xy}$	$+d_{xy}$	1.208^c	$+d_{xz}$	$-d_{xz}$			
SOMO−5	1.100^c	$+d_{x^2}$	$+d_{x^2}$						

[a] n indicates the electron occupation number. [b] Specified orbitals correspond to octahedral e_g orbitals. [c] Specified orbitals correspond to octahedral t_{2g} orbitals.

TABLE 9: Mn-Based Natural Orbitals of Mixed-Valence Complexes $[Mn_2O_2(H_2O)_8]^{q+}$ in the Lowest-Spin Configuration

natural orbital	**4a**			**4b**			**5**			**6**		
	n^a	Mn1	Mn2	n^a	Mn1	Mn2	n^a	Mn1	Mn2	n^a	Mn1	Mn2
LUMO+2										0.007^b		$+d_{z^2}$
LUMO+1							0.010^b		$+d_{z^2}$	0.012^b		$+d_{xy}$
LUMO	0.024^b		$+d_{xy}$	0.027^b		$+d_{xy}$	0.013^b		$+d_{xy}$	0.048^b	$+d_{xy}$	
SOMO+4	$0.869^{b,c}$	$+d_{x^2-z^2}$	$-d_{x^2}$	$0.874^{b,c}$	$+d_{x^2-z^2}$	$-d_{x^2}$						
SOMO+3	0.898^c	$+d_{xz}$	$+d_{xz}$	0.923^c	$+d_{xz}$	$+d_{xz}$	0.835^c	$+d_{xz}$	$+d_{xz}$	0.780^c	$+d_{xz}$	$+d_{xz}$
SOMO+2	0.936^c	$+d_{yz}$	$-d_{yz}$	$0.940^{b,c}$	$+d_{y^2}$	$+d_{y^2-z^2}$	$0.860^{b,c}$	$+d_{z^2}$	$+d_{x^2-y^2}$	$0.797^{b,c}$	$+d_{y^2-z^2}$	$-d_{x^2-y^2}$
SOMO+1	$0.944^{b,c}$	$+d_{y^2}$	$+d_{y^2-z^2}$	0.951^c	$+d_{yz}$	$-d_{yz}$	0.885^c	$+d_{yz}$	$-d_{yz}$	0.799^c	$+d_{yz}$	$-d_{yz}$
SOMO2							$1.0^{b,c}$	$+d_{xy}- d_{x^2-y^2}$				
SOMO1	1.0^b	$+d_{xy}$		1.0^b	$+d_{xy}$		$1.0^{b,c}$	$+d_{x^2-y^2} + d_{xy}$		$1.0^{b,c}$	$+dx^2 - d_{y^2-z^2}$	
SOMO−1	$1.056^{b,c}$	$+d_{y^2}$	$-d_{y^2-z^2}$	1.049^c	$+d_{yz}$	$+d_{yz}$	1.115^c	$+d_{yz}$	$+d_{yz}$	1.201^c	$+d_{yz}$	$+d_{yz}$
SOMO−2	1.064^c	$+d_{yz}$	$+d_{yz}$	$1.060^{b,c}$	$+d_{y^2}$	$-d_{y^2-z^2}$	$1.140^{b,c}$	$+d_{z^2}$	$-d_{x^2-y^2}$	$1.203^{b,c}$	$+d_{y^2-z^2}$	$+d_{x^2-y^2}$
SOMO−3	1.102^c	$+d_{xz}$	$-d_{xz}$	1.077^c	$+d_{xz}$	$-d_{xz}$	1.165^c	$+d_{xz}$	$-d_{xz}$	1.221^c	$+d_{xz}$	$-d_{xz}$
SOMO−4	$1.131^{b,c}$	$+d_{x^2-z^2}$	$+d_{x^2}$	$1.126^{b,c}$	$+d_{x^2-z^2}$	$+d_{x^2}$						

[a] n indicates the electron occupation number. [b] Specified orbitals correspond to octahedral e_g orbitals. [c] Specified orbitals correspond to octahedral t_{2g} orbitals.

doubly occupied electrons from the ligand to Mn, suggesting superexchange interactions through the di-μ-oxo bridge. Such covalent mixings are smaller for the Mn(II) ion than for Mn(III) and Mn(IV) ions because the Mn(II) ion has longer separations from ligands. The electron populations for minority-spin components in the octahedral t_{2g} and e_g orbitals of Mn(III) and Mn(IV) ions are respectively given as follows: 0.10, 0.10, and 0.12 (t_{2g}) and 0.26 and 0.11 (e_g) for Mn(III) in **2**; 0.17, 0.19, and 0.17 (t_{2g}) and 0.33 and 0.21 (e_g) for Mn(IV) in **3**; 0.14, 0.11, and 0.11 (t_{2g}) and 0.28 and 0.11 (e_g) for Mn(III) in **4a**; 0.10, 0.09, and 0.12 (t_{2g}) and 0.26 and 0.10 (e_g) for Mn(III) in **4b**; 0.27, 0.22, and 0.19 (t_{2g}) and 0.34 and 0.26 (e_g) for Mn(IV) in **5**; 0.08, 0.09, and 0.09 (t_{2g}) and 0.24 and 0.09 (e_g) for Mn(III) in **6**; 0.20, 0.21, and 0.21 (t_{2g}) and 0.33 and 0.25 (e_g) for Mn(IV) in **6**. These results indicate that the larger mixing arises for the d_{xy} component of octahedral e_g orbitals which are extended directly toward μ-oxo ions.

The Mulliken population analyses of $[Mn_2O_2(NH_3)_8]^{q+}$ in the Mn(III)−Mn(III), Mn(IV)−Mn(IV), and Mn(III)−Mn(IV) oxidation states have been reported in ref 30. The spin densities of $[Mn_2O_2(H_2O)_8]^{q+}$ in these oxidation states listed in Table 5 are consistent with those of $[Mn_2O_2(NH_3)_8]^{q+}$ as ±3.69 for Mn(III) in the Mn(III)−Mn(III) dimer, ±2.78 for Mn(IV) in the Mn(IV)−Mn(IV) dimer, and 3.71 for Mn(III) and −2.50 for Mn(IV) in the Mn(III)−Mn(IV) dimer, although the absolute values are somewhat smaller in $[Mn_2O_2(NH_3)_8]^{q+}$ than in $[Mn_2O_2(H_2O)_8]^{q+}$. The electron populations for majority- and minority-spin components of $[Mn_2O_2(NH_3)_8]^{q+}$ were given as follows: 0.99−1.00 and 0.14−0.15 (t_{2g}), 0.47 and 0.29 (d_{xy}), and 0.99 and 0.17 (d_{z^2}) for Mn(III) in the Mn(III)−Mn(III) center; 0.99 and 0.13−0.24 (t_{2g}), 0.51 and 0.37 (d_{xy}), and 0.49 and 0.35 (d_{z^2}) for Mn(IV) in the Mn(IV)−Mn(IV) center; 0.99−1.00 and 0.09−0.13 (t_{2g}), 0.50 and 0.30 (d_{xy}), 0.95 and 0.21 (d_{z^2}) for Mn(III) in the Mn(III)−Mn(IV) center; 0.99−1.00 and 0.25−0.26 (t_{2g}), 0.47 and 0.36 (d_{xy}), and 0.43 and 0.34 (d_{z^2}) for Mn(IV) in the Mn(III)−Mn(IV) center. In comparison with these gross orbital populations of $[Mn_2O_2(NH_3)_8]^{q+}$, the electron populations for minority-spin components seem to become slightly smaller in $[Mn_2O_2(H_2O)_8]^{q+}$ as shown in Tables 6 and 7, particularly for the octahedral e_g orbitals in the axial direction of the Mn(III)−Mn(IV) complex, suggesting that the orbital mixings between Mn and μ-oxo ions are smaller in the H_2O-coordinated complexes than in the NH_3-coordinated complexes.

VII. Natural Orbital Analysis of the Model Complex

We performed the natural orbital analysis of the model complexes to elucidate the singly occupied electron configurations of the Mn−Mn center in each oxidation state. The Mn-based natural orbitals of iso- and mixed-valence complexes in the lowest-spin configuration are listed in Tables 8 and 9, respectively, in which the main 3d orbitals with the largest components in Mulliken composition are given together with the electron occupation numbers. Figures 8 and 9, respectively, show the graphical presentations of the octahedral e_g natural orbitals of the iso- and mixed-valence complexes in the lowest-

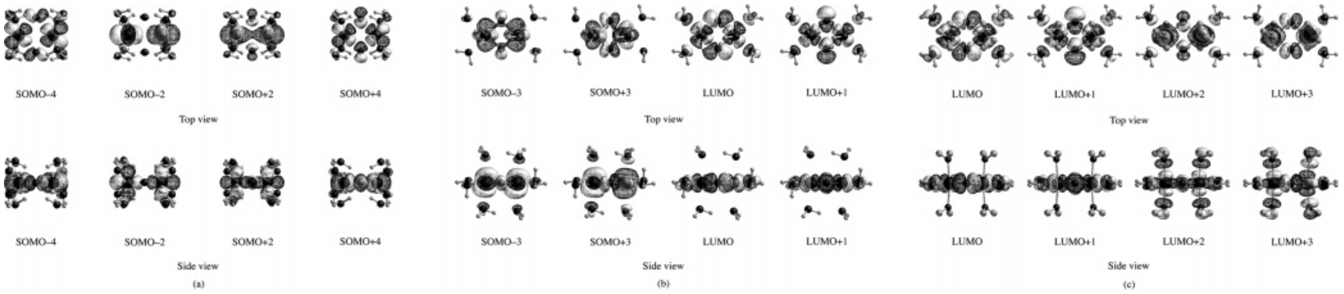

Figure 8. Octahedral e_g natural orbitals of iso-valence complexes in the lowest-spin state: (a) $Mn_2O_2(H_2O)_8$ (**1**), (b) $[Mn_2O_2(H_2O)_8]^{2+}$ (**2**), and (c) $[Mn_2O_2(H_2O)_8]^{4+}$ (**3**). Isocontours correspond to 0.025 au.

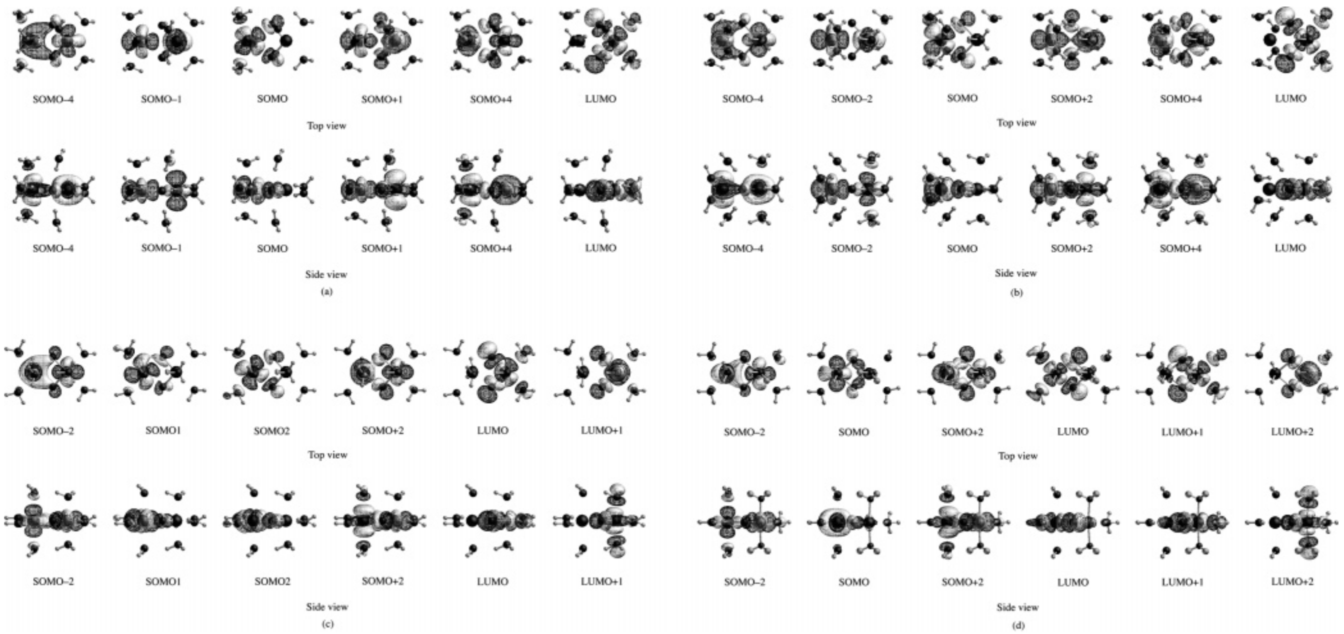

Figure 9. Octahedral e_g natural orbitals of mixed-valence complexes in the lowest-spin state: (a) $[Mn_2O_2(H_2O)_8]^+$ (**4a**), (b) $[Mn_2O_2(H_2O)_8]^+$ (**4b**), (c) $[Mn_2O_2(H_2O)_8]^{2+}$ (**5**), and (d) $[Mn_2O_2(H_2O)_8]^{3+}$ (**6**). Isocontours correspond to 0.025 au.

spin configuration, and it is confirmed from these Figures that the type of octahedral e_g orbital in the axial direction for each Mn site changes depending on the oxidation state of the Mn−Mn center as mentioned in the preceding section.

The pairs of Mn-based natural orbitals denoted as SOMO+m and SOMO−m, which give 2.0 as the sum of their electron occupation numbers, are composed of the in-phase and out-of-phase combinations between 3d orbitals centered at each Mn site, and these pairs form the broken-symmetry solutions of singlet-coupled biradicals. The pairings of d_{xz} and d_{yz} orbitals are common to **1**−**6**. The 3d components of SOMO1, SOMO2, LUMO, LUMO+1, and LUMO+2 for **4**−**6** are well localized at one of the Mn sites (Mn1 or Mn2). The SOMO1 and SOMO2 are the pure singly occupied orbitals with an electron occupation number of 1.0, and the SOMO for **4a** and **4b** is a nearly single 3d orbital of the Mn(II) site, whereas the SOMO for **5** and **6** has largely mixed 3d components within the same center of the Mn(II) or Mn(III) site (the SOMO1 and SOMO2 for **5** are the degenerate natural orbitals with $n = 1.0$).

The electron occupations of the octahedral e_g natural orbitals shown in Tables 8 and 9 change depending on the oxidation of the Mn−Mn center as follows: occupied d_{xy} (SOMO±4) and occupied $d_{y^2-z^2}$ (SOMO±2) for **1** with Mn(II)−Mn(II); occupied $d_{x^2-z^2}$ (SOMO±3) and unoccupied d_{xy} (LUMO and LUMO+1) for **2** with Mn(III)−Mn(III); unoccupied d_{xy} (LUMO and LUMO+1) and unoccupied d_{z^2} (LUMO+2 and LUMO+3) for **3** with Mn(IV)−Mn(IV); occupied $d_{x^2-z^2}$ on Mn1 (SOMO±4), occupied d_{xy} on Mn1 (SOMO), occupied $d_{y^2-z^2}$ on Mn2 (SOMO±1 for **4a** and SOMO±2 for **4b**), and unoccupied d_{xy} on Mn2 (LUMO) for **4** with Mn(II)−Mn(III); occupied d_{z^2} on Mn1 (SOMO±2), occupied d_{xy} on Mn1 (SOMO1 and SOMO2), unoccupied d_{xy} on Mn2 (LUMO), and unoccupied d_{z^2} on Mn2 (LUMO+1) for **5** with Mn(II)−Mn(IV); occupied $d_{y^2-z^2}$ on Mn1 (SOMO±2), unoccupied d_{xy} on Mn1 (LUMO), unoccupied d_{xy} on Mn2 (LUMO+1), and unoccupied d_{z^2} on Mn2 (LUMO+2) for **6** with Mn(III)−Mn(IV). However, the octahedral t_{2g} orbitals are always occupied in **1**−**6**. It is consequently confirmed that the one-electron oxidations of the Mn ion from Mn(II) to Mn(III) and from Mn(III) to Mn(IV) occur by removing occupied e_g electrons in the equatorial (d_{xy}) and axial (d_{z^2}) directions, respectively.

As seen in Figures 8 and 9, the equatorial e_g orbitals (SOMO±4 in Figure 8a, LUMO and LUMO+1 in Figures 8b and 8c, SOMO and LUMO in Figures 9a and 9b, SOMO1, SOMO2, and LUMO in Figure 9c, and LUMO and LUMO+1 in Figure 9d) indicate the antibonding character between Mn and μ-oxo ions and between the Mn ion and the equatorial H_2O ligand, whereas the axial e_g orbitals (SOMO±2 in Figure 8a, SOMO±3 in Figure 8b, LUMO+2 and LUMO+3 in Figure 8c, SOMO±4 in Figure 9a, SOMO±2 in Figure 9b, SOMO±2 and LUMO+1 in Figure 9c, and SOMO, SOMO±2, and LUMO+2 in Figure 9d) indicate the antibonding nature between the Mn ion and the axial H_2O ligand. Because the electron configurations of these orbitals vary according to the oxidation

TABLE 10: Experimental and Theoretical Effective Exchange Integrals of Iso- and Mixed-Valence Mn_2O_2 Complexes

oxidation state	$-J^a$	ref	oxidation state	$-J^a$	$\lvert B\rvert^b$	ref
	experiment			experiment		
Mn(III)−Mn(III)	86	30	Mn(III)−Mn(IV)	220		29
	87, 101	34		119−159		30
Mn(IV)−Mn(IV)	120	29		101−220		34
	126, 144	30				
	40−147	34				
	78−188	54				
	calculation			calculation		
Mn(II)−Mn(II)	2	this work	Mn(II)−Mn(III)	341, 337	293	this work
Mn(III)−Mn(III)	154	this work		23		34
	172	30	Mn(III)−Mn(IV)	1145	1821	this work
	176	33		405		29
	89	34		391	143	30
Mn(IV)−Mn(IV)	106	this work		268	135	33
	232	29		118		34
	274	30				
	125	31				
	118	32				
	99	32				
	149	32				
	129	33				
	101	34				
	124	53				
	115	53				

[a] Effective exchange integrals are given in cm^{-1}. [b] Resonance delocalization parameters are given in cm^{-1}.

states of complexes as described above such that both orbitals are occupied for Mn(II), the equatorial and axial orbitals are unoccupied and occupied for Mn(III), and both orbitals are unoccupied for Mn(IV), the deformations of molecular geometry with the oxidation of the Mn−Mn center would be induced for the Mn−ligand distances, which are essentially expected as Mn(II)−O > Mn(III)−O and Mn(IV)−O for the μ-oxo bridge, Mn(II)−OH_2 > Mn(III)−OH_2 and Mn(IV)−OH_2 for equatorial ligands, and Mn(II)−OH_2 and Mn(III)−OH_2 > Mn(IV)−OH_2 for axial ligands, corresponding to the optimized structures given in section V.

VIII. Magnetic Interaction of Model Complex

We summarize the experimental and theoretical J values of the Mn_2O_2 complexes with the di-μ-oxo bridge available from refs 29−34, 53, and 54 in Table 10 together with the J values of $[Mn_2O_2(H_2O)_8]^{q+}$ calculated in this work. The experimental values were measured for the complexes with various ligands (mainly N-donor). The theoretical values were calculated by the broken-symmetry DFT method for the following complexes: $[Mn_2O_2(OAc)(TACN)_2]^{2+}$ and $[Mn_2O_2(\mu\text{-}O_2)(TACN)_2]^{2+}$ in ref 29; $[Mn_2O_2(NH_3)_8]^{q+}$ in ref 30; $[Mn_2O_2(\mu\text{-}O_2)(NH_3)_6]^{2+}$ in ref 31; $[Mn_2O_2(pic)_4]$, $[Mn_2O_2(H_2O)_8]^{4+}$, and $[Mn_2O_2(NH_3)_8]^{4+}$ in ref 32; $[Mn_2O_2(O_2CH)(NH_3)_6]^{q+}$ in ref 33; $[Mn_2O_2(NH_3)_6(H_2O)_2]^{q+}$ in ref 34; $[Mn_2O_2(NHCHCO_2)_4]$ in ref 53. In our estimation of the J values for $[Mn_2O_2(H_2O)_8]^{q+}$, the iso-valence centers of Mn(II)−Mn(II), Mn(III)−Mn(III), and Mn(IV)−Mn(IV) and the mixed-valence centers of Mn(II)−Mn(III) and Mn(III)−Mn(IV) were examined, and the optimized structures of the highest- and lowest-spin configurations were used to obtain the J values as in ref 30. We performed the geometry optimizations with some of the geometrical constraints for the mixed-valence complexes **4** and **6** in the delocalized highest-spin state to take account of the delocalization effects for the J values (eq 8) in which an extra electron was placed in the in-phase or out-of-phase combinations of the d_{xy} orbitals on each Mn site for **4** and in those of the d_{z^2} orbitals on each Mn site for **6**, respectively. The calculated results of energies, geometries, and charge and spin densities of mixed-valence complexes in the delocalized highest-spin states are given in Appendix B.

As described in refs 49, 50, and 53 as examples, the theoretical J values largely depend on the computational methods such as the combination of the exchange and correlation functionals employed in DFT calculation. Thus, the J values of $[Mn_2O_2(H_2O)_8]^{q+}$ in the iso-valence oxidation state (**1**−**3**) listed in Table 10 would indicate that our results are consistent with the other theoretical results in the Mn(III)−Mn(III) and Mn(IV)−Mn(IV) oxidation states. In ref 32, it was shown that the theoretical $-J$ value of the Mn(IV)−Mn(IV) complex increases with ligands in the order H_2O ($-J = 99$ cm^{-1}) < pic ($-J = 118$ cm^{-1}) < NH_3 ($-J = 149$ cm^{-1}) in proportion to the number of coordinating N atoms, which is in accordance with the experimental tendency. The results obtained in this study therefore are consistent with the results of ref 32. Although the experimental and theoretical values of the Mn(II)−Mn(II) complex have not been reported, the J value calculated in this work is much smaller for **1** than for **2** and **3**, which would be caused by longer Mn(II)−Mn(II) and Mn(II)−O separations from a geometrical viewpoint, suggesting weak magnetic interactions.

The experimental results seem to show the relation of $-J$ for Mn(III)−Mn(III) < $-J$ for Mn(IV)−Mn(IV) in contrast to our result of $-J$ for Mn(III)−Mn(III) = 154 cm^{-1} > $-J$ for Mn(IV)−Mn(IV) = 106 cm^{-1}. However, it is noted that the experimental J values of the Mn(IV)−Mn(IV) complexes summarized in refs 34 and 54 indicate the following distribution of reported 28 and 20 data: 19 (ref 34) and 10 (ref 54) compounds in $-J < 100$ cm^{-1} and 9 (ref 34) and 10 (ref 54) compounds in 100 $cm^{-1} \leq -J$, whereas data of only three compounds have been given in refs 30 and 34 for the experimental J values of the Mn(III)−Mn(III) complexes as $-J \approx 90-100$ cm^{-1}. It is, thus, impossible to conclude exactly the order of experimental J values with overlap in the Mn(III)−Mn(III) and Mn(IV)−Mn(IV) oxidation states.

As for the mixed-valence complexes, Table 10 indicates that the $-J$ values are much larger in our calculations than in other theoretical and experimental work. (It is noted that the J values of the mixed-valence complexes reported in ref 34 may not include resonance delocalization effects.) However, it has been pointed out in refs 29, 48, and 52 that when the trapping energy ΔE_{trap} largely exceeds the resonance energy, $\Delta E_{\mathrm{trap}} \gg B(S + {}^1/_2)$, the observed J value would be given by $J_{\mathrm{eff}} = J + (B^2/\Delta E_{\mathrm{trap}})$ giving a positive (ferromagnetic) shift due to the partial delocalization, and the trapping energy is the same as the energy of the intervalence charge-transfer optical band, $\Delta E_{\mathrm{op}} = \Delta E_{\mathrm{trap}}$. Experimentally,[55−57] ΔE_{op} has been estimated as 7124 cm^{-1} for $[\mathrm{Mn(III)Mn(IV)}(\mu\text{-O})(\mathrm{OAc})_2(\mathrm{TACN})_2]^{3+}$ and 12 000 cm^{-1} for $[\mathrm{Mn(III)Mn(IV)O_2L_4}]^{3+}$ (L = 2,2′-bipyridine or 1,10-phenanthroline). We roughly estimate the $B^2/\Delta E_{\mathrm{trap}}$ value for $[\mathrm{Mn(III)Mn(IV)O_2(H_2O)_8}]^{3+}$ assuming that $\Delta E_{\mathrm{trap}} \approx$ 10 000 cm^{-1} to obtain a value of 332 cm^{-1}. (We note that the value of 9 cm^{-1} is obtained for $[\mathrm{Mn(II)Mn(III)O_2(H_2O)_8}]^{+}$ with the same assumption of $\Delta E_{\mathrm{trap}} \approx$ 10 000 cm^{-1}). The J values of $[\mathrm{Mn_2O_2(H_2O)_8}]^{q+}$ in the mixed-valence oxidation states (**4** and **6**) listed in Table 10 may be overestimated with uncertainties also because eq 8 is used for the fully delocalized limit of symmetric high-spin states, as discussed in ref 30. Moreover, the hydrogen bonds are formed in the broken-symmetry states of **4** and **6** as shown in Figures 5a, 5b, and 5d, whereas the hydrogen bonds in the delocalized high-spin states of **4** and **6** vanish or become weak with the longer bond lengths of 2.0−2.1 Å, indicating that the broken-symmetry states would be more stabilized by the hydrogen bonds that lead to large energy gaps between the highest- and lowest-spin configurations in the estimation of J values. In the case when the lower energy of delocalized highest-spin states is applied to eq 8 instead of the averaged energy of delocalized highest-spin states as the localized limit,[29,33] we obtain $-J$ values of 269 cm^{-1} for **4a**, 264 cm^{-1} for **4b**, and 555 cm^{-1} for **6**. However, if the resonance delocalization of the second term in eq 5 is ignored, and the localized highest-spin state of eq 4 is adopted for to the calculation of J values, the $-J$ values become 11 cm^{-1} for **4a**, 10 cm^{-1} for **4b**, and 163 cm^{-1} for **6**. The result for the Mn(III)−Mn(IV) complex **6** obtained from eq 4 seems to show similarity to the experimental values, suggesting a valence-trapped nature.

Here, we briefly discuss the superexchange pathways between the Mn sites through the di-μ-oxo bridge on the basis of the magnetic orbitals, which are obtained using eq 12 from the singlet-coupled natural orbitals of the broken-symmetry solutions. Figures 10 and 11 give graphical presentations of the singly occupied magnetic orbitals of the iso- and mixed-valence complexes, respectively, and the compositions of these orbitals are given in Appendix C. Although the compositions of the unrestricted canonical orbitals of $[\mathrm{Mn_2O_2(NH_3)_8}]^{q+}$ with the Mn(III)−Mn(III), Mn(III)−Mn(IV), and Mn(IV)−Mn(IV) centers were reported in ref 30, it may be impossible to compare the canonical orbitals directly with the magnetic orbitals. Because some of the 3d components of the Mn ions would be distributed over several canonical orbitals in a delocalized nature, it may be difficult to regard the specific canonical orbitals as singly occupied Mn 3d orbitals that characterize the magnetic properties of the molecule. It may therefore be reasonable to use the well-defined singly occupied orbitals such as the natural orbitals or the magnetic orbitals in the analysis of magnetic properties.[49−51,53]

Considering the interaction between Mn (parallel unpaired spins) and μ-oxo (closed shell) sites in the formal oxidation state, the contribution from the electron configuration, in which an electron of the μ-oxo ion with antiparallel spin to the electrons of the Mn ion that are transferred to one of the Mn ions, arises in the interacting system. The remaining spin on the μ-oxo bridge would induce a spin polarization with opposite direction on another Mn center. This leads to the antiparallel spin alignment between two Mn ions if another Mn ion has overlap interactions with the μ-oxo ions (superexchange interaction). Consequently, both orbital mixing between one Mn center and a di-μ-oxo bridge and the nonzero orbital overlap between the di-μ-oxo bridge and another Mn center are crucial for effective magnetic coupling by the superexchange mechanism.

The mixing weights of the di-μ-oxo bridge in the magnetic orbitals are smaller for the Mn(II) ion than for the Mn(III) and Mn(IV) ions with the exception of the d_{xy} orbital (Appendix C) as expected from the longer Mn−O distances for the Mn(II) site than for the Mn(III) and Mn(IV) sites. Because the d_{xy} orbital on the Mn(II) site, which faces the μ-oxo ion, interacts with the p_σ orbital of the μ-oxo bridge (SOMO±4 in Figure 10a for **1**, SOMO in Figures 9a and 9b for **4a** and **4b**, and SOMO1 and SOMO2 in Figure 9c for **5**), the d_{xy}/d_{xy} pathway may be considered to lead to the effective magnetic coupling through the di-μ-oxo bridge in the Mn(II)−Mn(II) complex. However, the d_{xy} orbital on the opposite Mn site would be nearly orthogonal to the bridging p_σ orbital, suggesting that the d_{xy}/d_{xy} pathway is inactive for the antiferromagnetic interaction between Mn(II) sites and the magnetic interactions are thus weaker in **1** with Mn(II)−Mn(II) than in **2** with Mn(III)−Mn(III) and **3** with Mn(IV)−Mn(IV). Less orbital mixing of 3d orbitals between both Mn site is found in the complexes including the Mn(II) ion of **1** with Mn(II)−Mn(II), **4a** and **4b** with Mn(II)−Mn(III), and **5** with Mn(II)−Mn(IV) (Appexdix C), indicating weak magnetic interactions also in these complexes.

The d_{xz}/d_{xz} and d_{yz}/d_{yz} pathways interacting with p_π orbital of the di-μ-oxo bridge are common to **2** with Mn(III)−Mn(III) and **3** with Mn(IV)−Mn(IV) (SOMO±4 and SOMO±2 in Figure 10b for **2** and SOMO±2 and SOMO±3 in Figure 10c for **3**). The d_{xz} and d_{yz} orbitals respectively indicate the 6 and 6% contributions in **2** and the 7 and 8% contributions in **3** from μ-oxo ions, the 2 and 1% mixings in **2** and the 3 and 3% mixings in **3** between Mn sites, and the localizabilities of 91 and 90% in **2** and 84 and 84% in **3**. However, in ref 30 the compositions of canonical orbitals were given as Mn/μ-oxo/Mn = 49:39:11 for the d_{xz} orbital and 54:30:7 for the d_{yz} orbital in $[\mathrm{Mn(III)_2O_2(NH_3)_8}]^{2+}$ and as Mn/μ-oxo/Mn = 35:48:15 for the d_{xz} orbital and 43:27:15 for the d_{yz} orbital in $[\mathrm{Mn(IV)_2O_2(NH_3)_8}]^{4+}$. Thus, it is found that the Mn-based orbitals are more delocalized in the canonical orbitals of $[\mathrm{Mn_2O_2(NH_3)_8}]^{q+}$ than in the magnetic orbitals of $[\mathrm{Mn_2O_2(H_2O)_8}]^{q+}$. The dependence of d_{xz}/d_{xz} and d_{yz}/d_{yz} pathways in $[\mathrm{Mn_2O_2(NH_3)_8}]^{q+}$ on the geometry of the $\mathrm{Mn_2O_2}$ core was also investigated in ref 30. The authors' conclusions state that the p_π orbital of the μ-oxo ion overlaps equally with the d_{xz} and d_{yz} orbitals at the point where the O−Mn−O angle is exactly 90°. As the O−Mn−O angle becomes narrow, the interaction between the p_π orbital and the d_{yz} orbital is enhanced and the interaction between the p_π orbital and the d_{xz} orbital is reduced, respectively. The antiferromagnetic contribution from the d_{yz}/d_{yz} pathway is, thus, enhanced at the optimized geometry, giving rise to a larger exchange coupling constant in $\mathrm{Mn(IV)_2}$ with O−Mn(IV)−O = 77.9° than in $\mathrm{Mn(III)_2}$ with O−Mn(III)−O = 84.8°. This trend would be true in the case of $[\mathrm{Mn_2O_2(H_2O)_8}]^{q+}$, although the difference in magnetic coupling between the d_{xz}/d_{xz} and d_{yz}/d_{yz} pathways may be small judging from the compositions of the d_{xz} and d_{yz} magnetic orbitals.

Regarding the remaining pathways of $d_{x^2-y^2}/d_{x^2-y^2}$ and d_{z^2}/d_{z^2} in the Mn(III)−Mn(III) and Mn(IV)−Mn(IV) centers, it was shown in ref 30 that these symmetric pathways do not contribute because of the absence of a direct orbital overlap between Mn

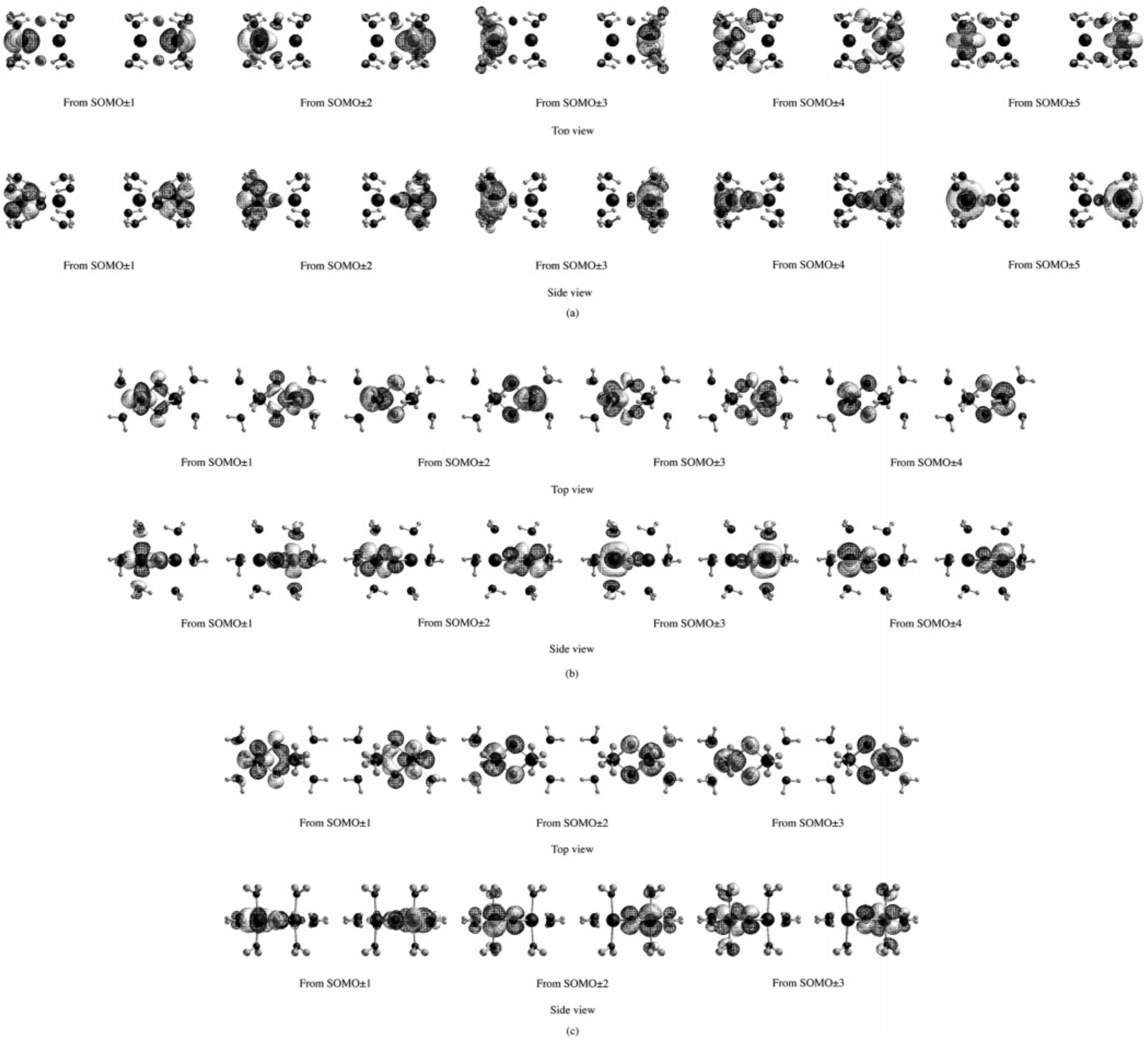

Figure 10. Singly occupied magnetic orbitals of iso-valence complexes in the lowest-spin configuration: (a) $Mn_2O_2(H_2O)_8$ (**1**), (b) $[Mn_2O_2(H_2O)_8]^{2+}$ (**2**), and (c) $[Mn_2O_2(H_2O)_8]^{4+}$ (**3**). Isocontours correspond to 0.025 au.

sites, whereas the crossed pathway of $d_{x^2-y^2}/d_{z^2}$ is possible with the compositions of canonical orbitals: Mn($d_{x^2-y^2}$)/μ-oxo/Mn(d_{z^2}) = 62:31:4 and Mn(d_{z^2})/μ-oxo/Mn($d_{x^2-y^2}$) = 61:5:5 in $[Mn(III)_2O_2(NH_3)_8]^{2+}$ and Mn($d_{x^2-y^2}$)/μ-oxo/Mn(d_{z^2}) = 60:25:5 in $[Mn(IV)_2O_2(NH_3)_8]^{4+}$. The authors of ref 30 concluded that the $d_{x^2-y^2}/d_{z^2}$ pathway makes only minor contributions to the overall exchange coupling constant in the Mn(III)−Mn(III) and Mn(IV)−Mn(IV) oxidation states, although it gives rise to additional antiferromagnetic (half filled $d_{x^2-y^2}$ and d_{z^2}) and ferromagnetic (half filled $d_{x^2-y^2}$ and vacant d_{z^2}) contributions in the $Mn(III)_2$ and $Mn(IV)_2$ dimers, respectively. However, the compositions of the magnetic orbitals of $[Mn_2O_2(H_2O)_8]^{q+}$ show that the $d_{x^2-z^2}/d_{x^2-z^2}$ and d_{y^2}/d_{y^2} pathways in **2** (SOMO±3 and SOMO±1 in Figure 10b) and the $d_{x^2-y^2}/d_{x^2-y^2}$ pathway in **3** (SOMO±1 in Figure 10(c) have small orbital mixings between Mn sites of 1 and 1% for $d_{x^2-z^2}$ and d_{y^2} orbitals in **2** and 2% for the $d_{x^2-y^2}$ orbital in **3**, whereas the crossed pathway seems to be absent although the orbital mixings on the same Mn center between $d_{x^2-z^2}$ and d_{y^2} in **2** and between $d_{x^2-y^2}$ and d_{z^2} in **3** are found. Therefore, these symmetric pathways are also expected to contribute secondly to the exchange coupling constant in addition to the dominant d_{xz}/d_{xz} and d_{yz}/d_{yz} pathways in the Mn(III)−Mn(III) and Mn(IV)−Mn(IV) centers of $[Mn_2O_2(H_2O)_8]^{q+}$, and it is suggested that the differences in contribution from the additional pathways may cause that $-J$ for **2** > $-J$ for **3** in contrast to that for $[Mn_2O_2(NH_3)_8]^{q+}$.

In the mixed-valence complex **6** with the Mn(III)−Mn(IV) center, the compositions of magnetic orbitals of Mn(III)/μ-oxo/Mn(IV) are given as follows: 84:2:2 and 2:13:74 for d_{xz} orbitals (SOMO±3 in Figure 11(d); 83:3:2 and 2:13:74 for d_{yz} orbitals (SOMO±1 in Figure 11(d); 52:2:3 and 1:12:61 for the $d_{y^2-z^2}$ orbital on Mn(III) and for the $d_{x^2-y^2}$ orbital on Mn(IV) (SOMO±2 in Figure 11d), respectively; 54:4:1 for the d_{x^2} orbital on Mn(III) (SOMO in Figure 9d). The SOMO and SOMO±2 indicate the orbital mixings within the same Mn site. The contributions from the d_{xz}/d_{xz} and d_{yz}/d_{yz} pathways to the exchange coupling constant would also be dominant in the mixed-valence complex of $[Mn(III)Mn(IV)O_2(H_2O)_8]^{3+}$ as in the iso-valence complexes of $[Mn(III)_2O_2(H_2O)_8]^{2+}$ and $[Mn(IV)_2O_2(H_2O)_8]^{4+}$. The SOMO and SOMO±2 indicate the

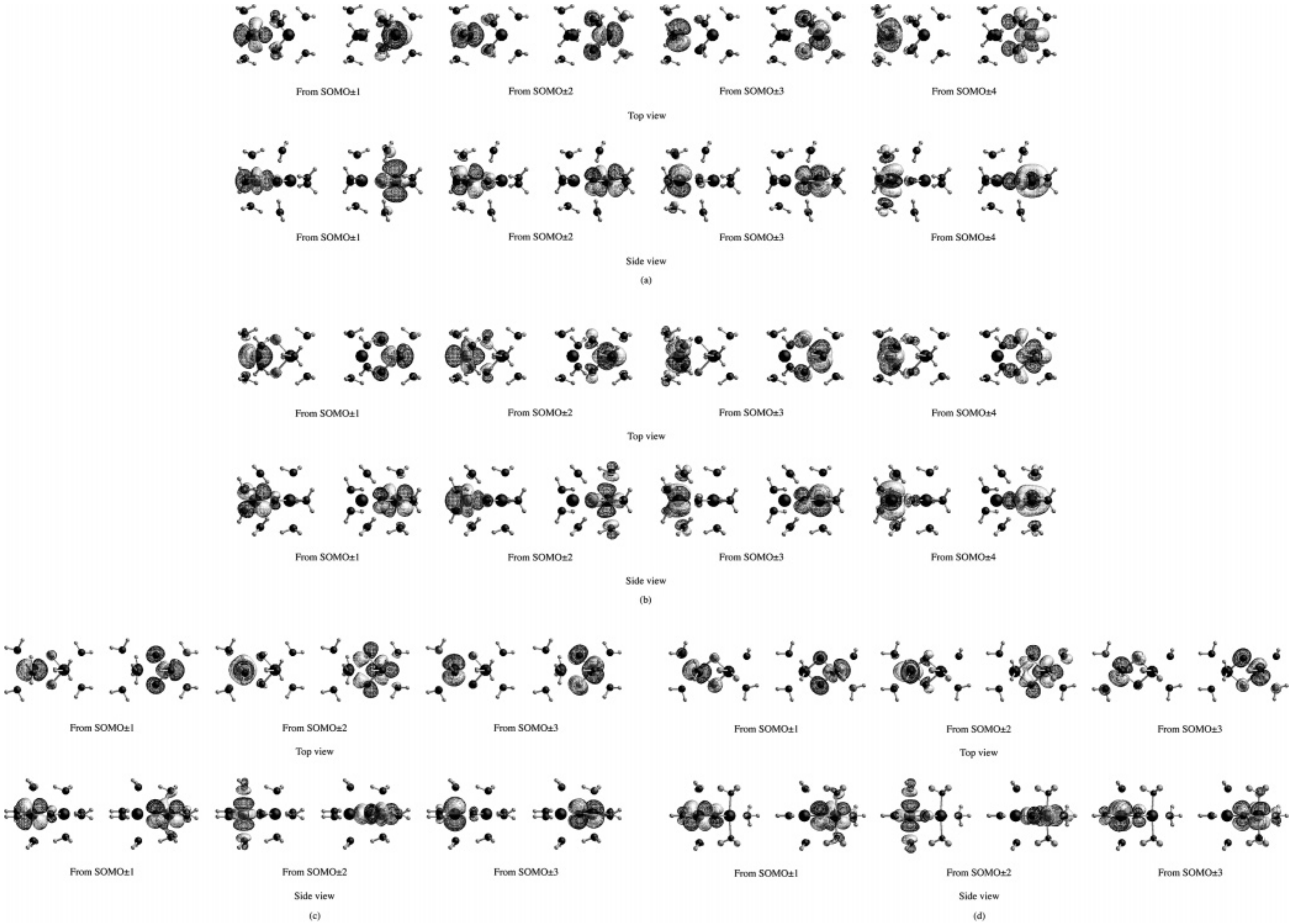

Figure 11. Singly occupied magnetic orbitals of mixed-valence complexes in the lowest-spin configuration: (a) $[Mn_2O_2(H_2O)_8]^+$ (**4a**), (b) $[Mn_2O_2(H_2O)_8]^+$ (**4b**), (c) $[Mn_2O_2(H_2O)_8]^{2+}$ (**5**), and (d) $[Mn_2O_2(H_2O)_8]^{3+}$ (**6**). Isocontours correspond to 0.025 au

orbital mixings among the d_{x^2} (Mn(III), $d_{y^2-z^2}$ Mn(III)), $d_{x^2-y^2}$ (Mn(IV)), and d_{z^2} (MN(IV)) components, suggesting the crossed pathway would be involved in these magnetic orbitals. The compositions of the canonical orbitals of $[Mn(III)Mn(IV)O_2(NH_3)_8]^{3+}$ given in ref 30 again show the delocalized nature as Mn(III)/μ-oxo/Mn(IV) = 46:34:20 and 8:45:46 for the d_{xz} orbitals, 48:21:15 and 7:34:48 for the d_{yz} orbitals, 57:20:14(d_{z^2}) and 4(d_{z^2}):28:64 for the $d_{x^2-y^2}$ orbitals, and 48(d_{z^2}):2:12($d_{x^2-y^2}$) for the unpaired orbital, indicating the crossed pathway of $d_{x^2-y^2}$/d_{z^2}.

IX. Summary

In the present study, we determined the stable geometries of di-μ-oxo-bridged Mn_2O_2 complexes with H_2O ligands $[Mn_2O_2(H_2O)_8]^{q+}$ ($q = 0-4$), the iso-valence complexes in the Mn(II)−Mn(II), Mn(III)−Mn(III), and Mn(IV)−Mn(IV) oxidation states, and the mixed-valence complexes in the Mn(II)−Mn(III), Mn(II)−Mn(IV), and Mn(III)−Mn(IV) oxidation states, using all-electron DFT calculation of the broken-symmetry B3LYP method, and the geometrical features and electronic structures were investigated in relation to their changes depending on the oxidation state of Mn−Mn center. The calculated results of $[Mn_2O_2(H_2O)_8]^{q+}$ in this study were compared with those of $[Mn_2O_2(NH_3)_8]^{q+}$ given in ref 30.

The antiparallel spin-couplings are energetically more stable than the parallel spin-couplings for the oxidation states without the Mn(II) ion, whereas the energy differences between both spin alignments in the oxidation states with the Mn(II) ion are small. Although the H_2O ligands of the Mn(III) and Mn(IV) sites are favorable to the octahedral positions, the H_2O ligands of the Mn(II) site indicate the tendency to move from the octahedral positions, which may be caused by the instability of octahedral positions at the Mn(II) site induced from the electron occupations of antibonding orbitals in the axial and equatorial directions. The formation of hydrogen bonds are found between axial H_2O ligands in the oxidation states except in Mn(II)−Mn(II) and Mn(IV)−Mn(IV) and between μ-oxo ions and H_2O ligands in the oxidation states of Mn(II)−Mn(II) and Mn(II)−Mn(III).

The optimized structures of $[Mn_2O_2(H_2O)_8]^{q+}$ are compatible with the reported structures of Mn_2O_2 complexes with various ligands, and the geometrical trends in the Mn_2O_2 core depending on the oxidation state of complexes are indicated as Mn(II)−O > Mn(III)−O ≈ Mn(IV)−O, O−Mn(II)−O > O−Mn(III)−O > O−Mn(IV)−O compared among iso-valence cores, and O−Mn(lower)−O < O−Mn(higher)−O compared within the mixed-valence core. The comparisons of interatomic distances between the model complexes optimized in this study and the cubanelike Mn cluster of the OEC observed in the recent X-ray crystallographic study would suggest that the Mn(II) ion may not be contained in the Mn_3CaO_4 structure.

The charge and spin densities are evaluated by the Mulliken population analysis, and the electron populations in the Mn 3d orbitals of $[Mn_2O_2(H_2O)_8]^{q+}$ seem to show correspondence with those of $[Mn_2O_2(NH_3)_8]^{q+}$ for the Mn(III)−Mn(III), Mn(IV)−Mn(IV), and Mn(III)−Mn(IV) oxidation states. The singly occupied electron configurations of the Mn−Mn center in each oxidation state are elucidated by the natural orbital analysis, and it is confirmed that the one-electron oxidations from Mn(II) to Mn(III) and from Mn(III) to Mn(IV), respectively, remove the octahedral e_g electrons in the equatorial (d_{xy}) and axial (d_{z^2}) orbitals.

The magnetic interactions between Mn sites through the μ-oxo bridge are examined from the estimation of effective exchange integrals and superexchange pathways. The J values of $[Mn_2O_2(H_2O)_8]^{q+}$ in the Mn(III)−Mn(III) and Mn(IV)−Mn(IV) oxidation states seem to be consistent with the other experimental and theoretical values, although the $-J$ value is slightly larger for the $Mn(III)_2$ dimer than for the $Mn(IV)_2$ dimer in contrast with that of $[Mn_2O_2(NH_3)_8]^{q+}$. The $-J$ value of $[Mn_2O_2(H_2O)_8]^{q+}$ in the Mn(II)−Mn(II) oxidation state becomes much smaller than that in the higher oxidation states, indicating weak magnetic interactions through longer Mn(II)−O separations. However, the J value of the mixed-valence complex with the Mn(III)−Mn(IV) center reveals a large deviation from the reported J values in other experimental and theoretical studies. Although the hydrogen bonds may affect the J value, it is impossible to conclude the magnitude of the J value exactly for $[Mn_2O_2(H_2O)_8]^{q+}$ in the Mn(III)−Mn(IV) oxidation state without uncertainty. The superexchange pathways of $[Mn_2O_2(H_2O)_8]^{q+}$ in the Mn(III)−Mn(III), Mn(IV)−Mn(IV), and Mn(III)−Mn(IV) oxidation states based on the Mulliken compositions of singly occupied magnetic orbitals suggest that the symmetric pathways of d_{xz}/d_{xz} and d_{yz}/d_{yz} are dominant, and the remaining symmetric pathways would also contribute to the

TABLE A1: Optimized Interatomic Distances in the Mn_2O_2 Core of Iso- and Mixed-Valence Complexes $[Mn_2O_2(H_2O)_8]^{q+}$

		interatomic distance (angströms)					
complex	S	Mn1−Mn2	O3−O4	Mn1−O3	Mn1−O4	Mn2−O3	Mn2−O4
1	10/2	2.948	2.949	2.085	2.084	2.084	2.086
	0/2	2.890	2.978	2.076	2.073	2.074	2.076
2	8/2	2.667	2.414	1.803	1.795	1.795	1.803
	0/2	2.651	2.397	1.790	1.784	1.784	1.790
3	6/2	2.748	2.302	1.792	1.793	1.793	1.793
	0/2	2.762	2.249	1.781	1.781	1.781	1.781
4a	9/2	2.840	2.622	2.127	2.128	1.753	1.754
	1/2	2.828	2.606	2.103	2.106	1.754	1.755
4b	9/2	2.830	2.639	2.085	2.085	1.794	1.794
	1/2	2.814	2.628	2.063	2.065	1.795	1.795
5	8/2	2.740	2.542	2.057	2.058	1.695	1.695
	2/2	2.749	2.517	2.048	2.048	1.694	1.694
6	7/2	2.696	2.356	1.827	1.829	1.748	1.757
	1/2	2.703	2.318	1.822	1.827	1.733	1.740

TABLE A2: Optimized Interatomic Angles in the Mn_2O_2 Core of Iso- and Mixed-Valence Complexes $[Mn_2O_2(H_2O)_8]^{q+}$

		interatomic angle (deg)			
complex	S	Mn1−O3−Mn2	Mn1−O4−Mn2	O3−Mn1−O4	O3−Mn2−O4
1	10/2	90.0	90.0	90.0	90.0
	0/2	88.3	88.3	91.7	91.7
2	8/2	95.7	95.7	84.3	84.3
	0/2	95.8	95.7	84.2	84.2
3	6/2	100.0	100.0	79.9	79.9
	0/2	101.7	101.7	78.3	78.3
4a	9/2	93.6	93.5	76.0	96.8
	1/2	93.9	93.7	76.5	95.9
4b	9/2	93.4	93.4	78.5	94.7
	1/2	93.4	93.4	79.0	94.0
5	8/2	93.3	93.3	76.3	97.2
	2/2	94.0	94.0	75.8	96.0
6	7/2	97.9	97.5	80.2	84.5
	1/2	98.9	98.5	78.9	83.7

TABLE A3: Optimized Interatomic Distances Between Mn Ions and H_2O Ligands of Iso- and Mixed-Valence Complexes $[Mn_2O_2(H_2O)_8]^{q+}$

		interatomic distance (angströms)							
complex	S	Mn1−O5[a]	Mn1−O6[a]	Mn2−O7[a]	Mn2−O8[a]	Mn1−O9[a]	Mn1−O10[a]	Mn2−O11[a]	Mn2−O12[a]
1	10/2	2.261	2.265	2.261	2.264	2.238	2.238	2.239	2.238
	0/2	2.268	2.269	2.266	2.270	2.244	2.245	2.244	2.244
2	8/2	2.414	2.255	2.255	2.413	2.092	2.089	2.090	2.093
	0/2	2.406	2.250	2.251	2.405	2.100	2.098	2.098	2.100
3	6/2	1.969	1.969	1.969	1.969	2.051	2.051	2.051	2.051
	0/2	1.968	1.968	1.968	1.968	2.049	2.049	2.049	2.049
4a	9/2	2.200	2.188	2.816	3.003	2.226	2.231	2.095	2.094
	1/2	2.196	2.184	2.779	2.959	2.241	2.245	2.096	2.095
4b	9/2	2.362	2.361	2.289	2.288	2.159	2.159	2.119	2.119
	1/2	2.384	2.379	2.284	2.284	2.165	2.165	2.122	2.122
5	8/2	2.350	2.350	2.010	2.010	2.180	2.180	2.163	2.164
	2/2	2.334	2.333	2.008	2.008	2.186	2.187	2.160	2.161
6	7/2	2.380	2.381	1.967	1.968	2.048	2.042	2.066	2.076
	1/2	2.356	2.357	1.969	1.969	2.058	2.051	2.066	2.072

[a] O5−O12 indicate O atoms in H_2O molecules shown in Figure 3, respectively.

exchange coupling constant, whereas the crossed pathway may be less important in the Mn dimers with H_2O ligands than in the Mn dimers with NH_3 ligands.

TABLE B1: Total and Relative Energies of the Mixed-Valence Complexes $[Mn_2O_2(H_2O)_8]^+$ and $[Mn_2O_2(H_2O)_8]^{3+}$ in the Delocalized Highest-Spin State

complex	S	$\langle \hat{S}^2 \rangle$	total energy (au)	relative energy (kcal/mol)
4	9/2	24.90	−3063.52301	0.00
	9/2	24.91	−3063.50964	8.38
6	7/2	16.05	−3062.70282	0.00
	7/2	16.12	−3062.63643	41.63

TABLE B2: Optimized Geometrical Parameters in the Mn_2O_2 Core of the Mixed-Valence Complexes $[Mn_2O_2(H_2O)]^+$ and $[Mn_2O_2(H_2O)_8]^{3+}$ in the Delocalized Highest-Spin State

complex	S	Mn−Mn[a]	O−O[a]	Mn−O[a]	O−Mn−O[b]
4	9/2	2.615	2.708	1.881, 1.883	92.0
	9/2	2.833	2.554	1.905, 1.909	84.0
6	7/2	2.683	2.374	1.790, 1.792	83.0
	7/2	2.794	2.291	1.805, 1.808	78.7

[a] Interatomic distances are given in angströms. [b] Interatomic angles are given in degrees.

Appendix A

The optimized geometrical parameters of iso- and mixed-valence complexes $[Mn_2O_2(H_2O)_8]^{q+}$ in the most-stable highest- and lowest-spin configurations are listed in Tables A1−A3 with Table A1 listing interatomic distances in the Mn_2O_2 core, Table A2 listing interatomic angles in the Mn_2O_2 core, and Table A3 listing interatomic distances between Mn ions and H_2O ligands.

Appendix B

We obtained the delocalized highest-spin states of mixed-valence complexes **4** and **6** by applying geometry optimization with constraints for some of the geometrical parameters. The calculated results of the total energies, Mn_2O_2 structures, and Mn_2O_2 charge and spin densities are summarized in Tables B1−B3, respectively.

Appendix C

The singly occupied magnetic orbitals of the iso- and mixed-valence complexes $[Mn_2O_2(H_2O)_8]^{q+}$ in the lowest-spin configuration are obtained from the singlet-coupled natural orbitals to recover the broken-symmetry picture. The Mulliken compositions of the magnetic orbitals of each complex are listed in

TABLE B3: Mulliken Charge and Spin Densities on Atoms in the Mn_2O_2 Core of the Mixed-Valence Complexes $[Mn_2O_2(H_2O)_8]^+$ and $[Mn_2O_2(H_2O)_8]^{3+}$ in the Delocalized Highest-Spin State

		charge density				spin density			
complex	S	Mn1	Mn2	O3	O4	Mn1	Mn2	O3	O4
4	9/2	1.401	1.401	−1.058	−1.058	4.350	4.350	0.062	0.062
	9/2	1.415	1.415	−1.060	−1.060	4.396	4.394	0.044	0.044
6	7/2	1.658	1.658	−0.747	−0.747	3.581	3.580	−0.132	−0.132
	7/2	1.675	1.675	−0.784	−0.783	3.597	3.597	−0.089	−0.091

TABLE C1: Mulliken Compositions of the Singly Occupied Magnetic Orbitals of the Iso-Valence Complex $Mn_2O_2(H_2O)_8$ (1) in the Lowest-Spin Configuration

magnetic orbital[a]	W1 (eq)[b]	W1 (ax)[b]	Mn1[c]						OO[d]	Mn2[c]						W2 (ax)[e]	W2 (eq)[e]
			sp	d_{xz}	d_{yz}	d_{x^2}	d_{xy}	$d_{y^2-z^2}$		sp	d_{xz}	d_{yz}	d_{x^2}	d_{xy}	$d_{y^2-z^2}$		
SOMO±1 (+)	0	0	0	0	0	0	0	0	1	0	0	97	0	0	0	1	1
SOMO±1 (−)	1	1	0	0	97	0	0	0	1	0	0	0	0	0	0	0	0
SOMO±2 (+)	0	2	0	2	0	23	0	71	2	0	0	0	0	0	0	0	0
SOMO±2 (−)	0	0	0	0	0	0	0	0	2	0	2	0	23	0	71	2	0
SOMO±3 (+)	2	2	0	92	0	0	0	3	1	0	0	0	0	0	0	0	0
SOMO±3 (−)	0	0	0	0	0	0	0	0	1	0	92	0	0	0	3	2	2
SOMO±4 (+)	1	0	0	0	0	0	0	0	7	0	0	0	0	89	0	1	2
SOMO±4 (−)	2	1	0	0	0	0	89	0	7	0	0	0	0	0	0	0	1
SOMO±5 (+)	0	1	2	1	0	72	0	23	2	0	0	0	0	0	0	0	0
SOMO±5 (−)	0	0	0	0	0	0	0	0	2	2	1	0	72	0	23	1	0

[a] SOMO±*m* (+) and SOMO±*m* (−) correspond to plus and minus mixings of SOMO+*m* and SOMO−*m*, respectively. [b] W1 (ax) and W1 (eq) indicate axial and equatorial H_2O molecules coordinated to Mn1, respectively. [c] The first three and last two 3d orbitals correspond to the octahedral t_{2g} and e_g orbitals, respectively. [d] OO indicates a di-μ-oxo bridge between Mn1 and Mn2. [e] W2 (ax) and W2 (eq) indicate axial and equatorial H_2O molecules coordinated to Mn2, respectively.

TABLE C2: Mulliken Compositions of the Singly Occupied Magnetic Orbitals of the Iso-Valence Complex $[Mn_2O_2(H_2O)_8]^{2+}$ (2) in the Lowest-Spin Configuration

magnetic orbital[a]	W1 (eq)[b]	W1 (ax)[b]	Mn1[c]						OO[d]	Mn2[c]						W2 (ax)[e]	W2 (eq)[e]
			sp	d_{xz}	d_{yz}	d_{y^2}	d_{xy}	$d_{x^2-z^2}$		sp	d_{xz}	d_{yz}	d_{y^2}	d_{xy}	$d_{x^2-z^2}$		
SOMO±1 (+)	1	2	1	0	0	85	0	4	5	0	0	0	1	0	0	0	0
SOMO±1 (−)	0	0	0	0	0	1	0	0	5	1	0	0	85	0	4	2	1
SOMO±2 (+)	0	0	0	0	1	0	0	0	6	0	0	90	1	0	2	0	1
SOMO±2 (−)	1	1	0	0	90	0	0	2	6	0	0	1	0	0	0	0	0
SOMO±3 (+)	0	0	0	0	0	0	0	1	5	1	0	2	4	0	83	3	1
SOMO±3 (−)	1	3	1	0	2	4	0	83	5	0	0	0	0	0	1	0	0
SOMO±4 (+)	1	0	0	91	0	0	0	0	6	0	2	0	0	0	0	0	0
SOMO±4 (−)	0	0	0	2	0	0	0	0	6	0	91	0	0	0	0	0	1

[a] SOMO±*m* (+) and SOMO±*m* (−) correspond to plus and minus mixings of SOMO+*m* and SOMO−*m*, respectively. [b] W1 (ax) and W1 (eq) indicate axial and equatorial H_2O molecules coordinated to Mn1, respectively. [c] The first three and last two 3d orbitals correspond to the octahedral t_{2g} and e_g orbitals, respectively. [d] OO indicates a di-μ-oxo bridge between Mn1 and Mn2. [e] W2 (ax) and W2 (eq) indicate axial and equatorial H_2O molecules coordinated to Mn2, respectively.

TABLE C3: Mulliken Compositions of the Singly Occupied Magnetic Orbitals of the Iso-Valence Complex $[Mn_2O_2(H_2O)_8]^{4+}$ (3) in the Lowest-Spin Configuration

magnetic orbital[a]	W1 (eq)[b]	W1 (ax)[b]	Mn1[c]						OO[d]	Mn2[c]						W2 (ax)[e]	W2 (eq)[e]
			sp	d_{xz}	d_{yz}	$d_{x^2-y^2}$	d_{xy}	d_{z^2}		sp	d_{xz}	d_{yz}	$d_{x^2-y^2}$	d_{xy}	d_{z^2}		
SOMO±1 (+)	1	0	0	0	0	64	0	26	6	0	0	0	2	0	0	0	0
SOMO±1 (−)	0	0	0	0	0	2	0	0	6	0	0	0	64	0	26	0	1
SOMO±2 (+)	2	2	0	84	0	0	0	2	7	0	3	0	0	0	0	0	0
SOMO±2 (−)	0	0	0	3	0	0	0	0	7	0	84	0	0	0	2	2	2
SOMO±3 (+)	0	1	0	0	3	0	0	0	8	0	0	84	0	0	0	4	2
SOMO±3 (−)	2	4	0	0	84	0	0	0	8	0	0	3	0	0	0	1	0

[a] SOMO±*m* (+) and SOMO±*m* (−) correspond to plus and minus mixings of SOMO+*m* and SOMO−*m*, respectively. [b] W1 (ax) and W1 (eq) indicate axial and equatorial H_2O molecules coordinated to Mn1, respectively. [c] The first three and last two 3d orbitals correspond to the octahedral t_{2g} and e_g orbitals, respectively. [d] OO indicates a di-μ-oxo bridge between Mn1 and Mn2. [e] W2 (ax) and W2 (eq) indicate axial and equatorial H_2O molecules coordinated to Mn2, respectively.

TABLE C4: Mulliken Compositions of the Singly Occupied Magnetic Orbitals of the Mixed-Valence Complex $[Mn_2O_2(H_2O)_8]^{+}$ (4a) in the Lowest-Spin Configuration

magnetic orbital[a]	W1 (eq)[b]	W1 (ax)[b]	Mn1[c]						OO[d]	Mn2[c]						W2 (ax)[e]	W2 (eq)[e]
			sp	d_{xz}	d_{yz}	d_{y^2}	d_{xy}	$d_{x^2-z^2}$		sp	d_{xz}	d_{yz}	d_{x^2}	d_{xy}	$d_{y^2-z^2}$		
SOMO[f]	2	0	0	1	8	0	82	0	6	0	0	0	0	0	0	0	1
SOMO±1 (+)	0	0	0	0	0	0	0	0	3	6	0	0	38	0	51	1	0
SOMO±1 (−)	1	0	0	0	0	92	0	4	2	0	0	0	0	0	0	0	0
SOMO±2 (+)	0	0	0	0	0	0	0	0	8	0	0	89	0	0	0	1	1
SOMO±2 (−)	0	1	0	1	88	0	7	1	2	0	0	0	0	0	0	0	0
SOMO±3 (+)	0	0	0	0	0	0	0	0	11	0	86	0	0	0	0	1	1
SOMO±3 (−)	1	1	0	96	0	0	1	0	1	0	1	0	0	0	0	0	0
SOMO±4 (+)	0	0	1	0	0	0	0	0	10	2	0	0	46	0	38	0	1
SOMO±4 (−)	1	4	0	0	1	4	0	89	1	0	0	0	1	0	0	0	0

[a] SOMO±*m* (+) and SOMO±*m* (−) correspond to plus and minus mixings of SOMO+*m* and SOMO−*m*, respectively. [b] W1 (ax) and W1 (eq) indicate axial and equatorial H_2O molecules coordinated to Mn1, respectively. [c] The first three and last two 3d orbitals correspond to the octahedral t_{2g} and e_g orbitals, respectively. [d] OO indicates a di-μ-oxo bridge between Mn1 and Mn2. [e] W2 (ax) and W2 (eq) indicate axial and equatorial H_2O molecules coordinated to Mn2, respectively. [f] Compositions of the natural orbital are shown.

TABLE C5: Mulliken Compositions of the Singly Occupied Magnetic Orbitals of the Mixed-Valence Complex $[Mn_2O_2(H_2O)_8]^{+}$ (4b) in the Lowest-Spin Configuration

magnetic orbital[a]	W1 (eq)[b]	W1 (ax)[b]	Mn1[c]						OO[d]	Mn2[c]						W2 (ax)[e]	W2 (eq)[e]
			sp	d_{xz}	d_{yz}	d_{y^2}	d_{xy}	$d_{x^2-z^2}$		sp	d_{xz}	d_{yz}	d_{x^2}	d_{xy}	$d_{y^2-z^2}$		
SOMO[f]	2	0	0	0	0	0	89	0	8	0	0	0	0	0	0	0	1
SOMO±1 (+)	0	1	0	0	0	0	0	0	6	0	0	92	0	0	0	1	1
SOMO±1 (−)	1	0	0	0	97	0	0	0	1	0	0	0	0	0	0	0	0
SOMO±2 (+)	0	0	0	0	0	0	0	0	4	1	1	0	25	0	64	4	1
SOMO±2 (−)	1	1	0	1	0	95	0	0	3	0	0	0	0	0	0	0	0
SOMO±3 (+)	2	2	1	87	0	1	0	6	1	0	0	0	0	0	0	0	0
SOMO±3 (−)	0	1	0	0	0	0	0	0	7	0	86	0	2	0	3	0	1
SOMO±4 (+)	0	0	0	0	0	0	0	1	7	1	4	0	60	0	24	2	1
SOMO±4 (−)	1	1	1	7	0	0	0	89	1	0	0	0	0	0	0	0	0

[a] SOMO±*m* (+) and SOMO±*m* (−) correspond to plus and minus mixings of SOMO+*m* and SOMO−*m*, respectively. [b] W1 (ax) and W1 (eq) indicate axial and equatorial H_2O molecules coordinated to Mn1, respectively. [c] The first three and last two 3d orbitals correspond to the octahedral t_{2g} and e_g orbitals, respectively. [d] OO indicates a di-μ-oxo bridge between Mn1 and Mn2. [e] W2 (ax) and W2 (eq) indicate axial and equatorial H_2O molecules coordinated to Mn2, respectively. [f] Compositions of the natural orbital are shown.

TABLE C6: Mulliken Compositions of the Singly Occupied Magnetic Orbitals of the Mixed-Valence Complex $[Mn_2O_2(H_2O)_8]^{2+}$ (5) in the Lowest-Spin Configuration

magnetic orbital[a]	W1 (eq)[b]	W1 (ax)[b]	Mn1[c]						OO[d]	Mn2[c]						W2 (ax)[e]	W2 (eq)[e]
			sp	d_{xz}	d_{yz}	$d_{x^2-y^2}$	d_{xy}	d_{z^2}		sp	d_{xz}	d_{yz}	$d_{x^2-y^2}$	d_{xy}	d_{z^2}		
SOMO1[f]	2	0	0	0	0	46	35	12	4	0	0	0	0	0	0	0	0
SOMO2[f]	2	0	0	0	0	31	54	8	5	0	0	0	0	0	0	0	0
SOMO±1 (+)	0	0	0	0	1	0	0	0	17	0	0	80	0	0	0	2	1
SOMO±1 (−)	1	0	0	0	97	0	0	0	1	0	0	1	0	0	0	0	0
SOMO±2 (+)	1	3	1	3	0	19	0	73	1	0	0	0	1	0	0	0	0
SOMO±2 (−)	0	0	1	0	0	0	0	1	14	0	2	0	71	0	10	0	1
SOMO±3 (+)	0	0	0	1	0	0	0	0	23	0	73	0	2	0	0	1	0
SOMO±3 (−)	1	0	0	95	0	0	0	2	0	0	1	0	0	0	0	0	0

[a] SOMO±*m* (+) and SOMO±*m* (−) correspond to plus and minus mixings of SOMO+*m* and SOMO−*m*, respectively. [b] W1 (ax) and W1 (eq) indicate axial and equatorial H_2O molecules coordinated to Mn1, respectively. [c] The first three and last two 3d orbitals correspond to the octahedral t_{2g} and e_g orbitals, respectively. [d] OO indicates a di-μ-oxo bridge between Mn1 and Mn2. [e] W2 (ax) and W2 (eq) indicate axial and equatorial H_2O molecules coordinated to Mn2, respectively. [f] Compositions of the natural orbital are shown.

TABLE C7: Mulliken Compositions of the Singly Occupied Magnetic Orbitals of the Mixed-Valence Complex $[Mn_2O_2(H_2O)_8]^{3+}$ (6) in the Lowest-Spin Configuration

magnetic orbital[a]	W1 (eq)[b]	W1 (ax)[b]	Mn1[c]						OO[d]	Mn2[c]						W2 (ax)[e]	W2 (eq)[e]
			sp	d_{xz}	d_{yz}	d_{x^2}	d_{xy}	$d_{y^2-z^2}$		sp	d_{xz}	d_{yz}	$d_{x^2-y^2}$	d_{xy}	d_{z^2}		
SOMO[f]	1	1	0	0	0	54	0	40	4	0	0	0	0	0	1	0	0
SOMO±1 (+)	0	0	0	0	2	0	0	0	13	0	9	74	0	0	0	2	1
SOMO±1 (−)	1	0	0	10	83	0	0	0	3	0	0	2	0	0	0	0	0
SOMO±2 (+)	1	4	1	0	0	37	0	52	2	0	0	0	2	0	1	0	0
SOMO±2 (−)	0	0	0	0	0	0	0	1	12	0	0	0	61	0	23	0	1
SOMO±3 (+)	0	0	0	2	0	0	0	0	13	0	74	8	0	0	0	1	1
SOMO±3 (−)	2	0	0	84	10	0	0	0	2	0	2	0	0	0	0	0	0

[a] SOMO±*m* (+) and SOMO±*m* (−) correspond to plus and minus mixings of SOMO+*m* and SOMO−*m*, respectively. [b] W1 (ax) and W1 (eq) indicate axial and equatorial H_2O molecules coordinated to Mn1, respectively. [c] The first three and last two 3d orbitals correspond to the octahedral t_{2g} and e_g orbitals, respectively. [d] OO indicates a di-μ-oxo bridge between Mn1 and Mn2. [e] W2 (ax) and W2 (eq) indicate axial and equatorial H_2O molecules coordinated to Mn2, respectively. [f] Compositions of the natural orbital are shown.

Tables C1−C7 as Table C1 for **1**, Table C2 for **2**, Table C3 for **3**, Table C4 for **4a**, Table C5 for **4b**, Table C6 for **5**, and Table C7 for **6**.

References and Notes

(1) Messinger, J. *Biochim. Biophys. Acta* **2000**, *1459*, 481−488.

(2) Siegbahn, P. E. M. *Inorg. Chem.* **2000**, *39*, 2923−2935.

(3) Siegbahn, P. E. M.; Crabtree, R. H. *Struct. Bonding* **2000**, *97*, 125−144.

(4) Robblee, J. H.; Cinco, R. M.; Yachandra, V. K. *Biochim. Biophys. Acta* **2001**, *1503*, 7−23.

(5) Dau, H.; Iuzzolino, L.; Dittmer, J. *Biochim. Biophys. Acta* **2001**, *1503*, 24−39.

(6) Nugent, J. H. A.; Rich, A. M.; Evans, M. C. W. *Biochim. Biophys. Acta* **2001**, *1503*, 138−146.

(7) Carrell, T. G.; Tyryshkin, A. M.; Dismukes, G. C. *J. Biol. Inorg. Chem.* **2002**, *7*, 2−22.

(8) Barber, J. *Curr. Opin. Struct. Biol.* **2002**, *12*, 523−530.

(9) Siegbahn, P. E. M. *Curr. Opin. Chem. Biol.* **2002**, *6*, 227−235.

(10) Blomberg, M. R. A.; Siegbahn, P. E. M. *Mol. Phys.* **2003**, *101*, 323−333.

(11) Lundberg, M.; Blomberg, M. R. A.; Siegbahn, P. E. M. *Theor. Chem. Acc.* **2003**, *110*, 130−143.

(12) Siegbahn, P. E. M.; Blomberg, M. R. A. *Biochim. Biophys. Acta* **2004**, *1655*, 45−50.

(13) Barber, J. *Biochim. Biophys. Acta* **2004**, *1655*, 123−132.

(14) Sauer, K.; Yachandra, V. K. *Biochim. Biophys. Acta* **2004**, *1655*, 140−148.

(15) Britt, R. D.; Campbell, K. A.; Peloquin, J. M.; Gilchrist, M. L.; Aznar, C. P.; Dicus, M. M.; Robblee, J.; Messinger, J. *Biochim. Biophys. Acta* **2004**, *1655*, 158−171.

(16) Pace, R. J.; Åhrling, K. A. *Biochim. Biophys. Acta* **2004**, *1655*, 172−178.

(17) Zouni, A.; Witt, H.-T.; Kern, J.; Fromme, P.; Krauss, N.; Saenger, W.; Orth, P. *Nature* **2001**, *409*, 739−743.

(18) Kamiya, N.; Shen, J.-R. *Proc. Natl. Acad. Sci. U.S.A.* **2003**, *100*, 98−103.

(19) Ferreira, K. N.; Iverson, T. M.; Maghlaoui, K.; Barber, J.; Iwata, S. *Science* **2004**, *303*, 1831−1838.

(20) Biesiadka, J.; Loll, B.; Kern, J.; Irrgang, K.-D.; Zouni, A. *Phys. Chem. Chem. Phys.* **2004**, *6*, 4733−4736.

(21) Loll, B.; Kern, J.; Saenger, W.; Zouni, A.; Biesiadka, J. *Nature* **2005**, *438*, 1040−1044.

(22) Iwata, S.; Barber, J. *Curr. Opin. Struct. Biol.* **2004**, *14*, 447−453.

(23) Barber, J.; Ferreira, K.; Maghlaoui, K.; Iwata, S. *Phys. Chem. Chem. Phys.* **2004**, *6*, 4737−4742.

(24) McEvoy, J. P.; Brudvig, G. W. *Phys. Chem. Chem. Phys.* **2004**, *6*, 4754−4763.

(25) Messinger, J. *Phys. Chem. Chem. Phys.* **2004**, *6*, 4764−4771.

(26) Dasgupta, J.; van Willigen, R. T.; Dismukes, G. C. *Phys. Chem. Chem. Phys.* **2004**, *6*, 4793−4802.

(27) Dau, H.; Liebisch, P.; Haumann, M. *Phys. Chem. Chem. Phys.* **2004**, *6*, 4781−4792.

(28) Proserpio, D. M.; Hoffmann, R.; Dismukes, G. C. *J. Am. Chem. Soc.* **1992**, *114*, 4374−4382.

(29) Zhao, X. G.; Richardson, W. H.; Chen, J.-L.; Li, J.; Noodleman, L; Tsai, H.-L.; Hendrickson, D. N. *Inorg. Chem.* **1997**, *36*, 1198−1217.

(30) McGrady, J. E.; Stranger, R. *J. Am. Chem. Soc.* **1997**, *119*, 8512−8522.

(31) McGrady, J. E.; Stranger, R. *Inorg. Chem.* **1999**, *38*, 550−558.

(32) Soda, T.; Kitagawa, Y.; Onishi, T.; Takano, Y.; Yoshioka, Y.; Yamaguchi, K. *Mol. Cryst. Liq. Cryst.* **2000**, *343*, 157−162.

(33) Delfs, C. D.; Stranger, R. *Inorg. Chem.* **2001**, *40*, 3061−3076.

(34) Aullón, G.; Ruiz, E.; Alvarez, S. *Chem.*−*Eur. J.* **2002**, *8*, 2508−2515.

(35) Delfs, C. D.; Stranger, R. *Inorg. Chem.* **2003**, *42*, 2495−2503.

(36) Lundberg, M.; Blomberg, M. R. A.; Siegbahn, P. E. M. *Inorg. Chem.* **2004**, *43*, 264−274.

(37) Petrie, S.; Stranger, R. *Inorg. Chem.* **2004**, *43*, 5237−5244.

(38) Petrie, S.; Mukhopadhyay, S.; Armstrong, W. H.; Stranger, R. *Phys. Chem. Chem. Phys.* **2004**, *6*, 4871−4877.

(39) Lundberg, M.; Siegbahn, P. E. M. *Phys. Chem. Chem. Phys.* **2004**, *6*, 4772−4780.

(40) Isobe, H.; Shoji, M.; Koizumi, K.; Kitagawa, Y.; Yamanaka, S.; Kuramitsu, S.; Yamaguchi, K. *Polyhedron* **2005**, *24*, 2767−2777.

(41) Mitani, M.; Katsurada, T.; Wakamatsu, Y.; Yoshioka, Y. *Internet Electron. J. Mol. Des.* **2005**, *4*, 94−105.

(42) Hay, P. J.; Wadt, W. R. *J. Chem. Phys.* **1985**, *82*, 270−283.

(43) Becke, A. D. *J. Chem. Phys.* **1993**, *98*, 5648−5652.

(44) Lee, C.; Yang, W.; Parr, R. G. *Phys. Rev. B* **1988**, *37*, 785−789.

(45) Schäfer, A.; Horn, H.; Ahlrichs, R. *J. Chem. Phys.* **1992**, *97*, 2571−2577.

(46) Hariharan, P. C.; Pople, J. A. *Theor. Chim. Acta* **1973**, *28*, 213−222.

(47) Frisch, M. J.; Trucks, G. W.; Schlegel, H. B.; Scuseria, G. E.; Robb, M. A.; Cheeseman, J. R.; Zakrzewski, V. G.; Montgomery, J. A., Jr.; Stratmann, R. E.; Burant, J. C.; Dapprich, S.; Millam, J. M.; Daniels, A. D.; Kudin, K. N.; Strain, M. C.; Farkas, O.; Tomasi, J.; Barone, V.; Cossi, M.; Cammi, R.; Mennucci, B.; Pomelli, C.; Adamo, C.; Clifford, S.; Ochterski, J.; Petersson, G. A.; Ayala, P. Y.; Cui, Q.; Morokuma, K.; Malick, D. K.; Rabuck, A. D.; Raghavachari, K.; Foresman, J. B.; Cioslowski, J.; Ortiz, J. V.; Stefanov, B. B.; Liu, G.; Liashenko, A.; Piskorz, P.; Komaromi, I.; Gomperts, R.; Martin, R. L.; Fox, D. J.; Keith, T.; Al-Laham, M. A.; Peng, C. Y.; Nanayakkara, A.; Gonzalez, C.; Challacombe, M.; Gill, P. M. W.; Johnson, B. G.; Chen, W.; Wong, M. W.; Andres, J. L.; Head-Gordon, M.; Replogle, E. S.; Pople, J. A. *Gaussian 98*, revision A.6; Gaussian, Inc.: Pittsburgh, PA, 1998.

(48) Noodleman, L.; Case, D. A. *Adv. Inorg. Chem.* **1992**, *38*, 423−470.

(49) Nagao, H.; Nishino, M.; Shigeta, Y.; Soda, T.; Kitagawa, Y.; Onishi, T.; Yoshioka, Y.; Yamaguchi, K. *Coord. Chem. Rev.* **2000**, *198*, 265−295.

(50) Shoji, M.; Nishiyama, Y.; Maruno, Y.; Koizumi, K.; Kitagawa, Y.; Yamanaka, S.; Kawakami, T.; Okumura, M.; Yamaguchi, K. *Int. J. Quantum Chem.* **2004**, *100*, 887−906.

(51) Shoji, M.; Koizumi, K.; Kitagawa, Y.; Yamanaka, S.; Kawakami, T.; Okumura, M.; Yamaguchi, K. *Int. J. Quantum Chem.* **2005**, *105*, 628−644.

(52) Blondin, G.; Girerd, J.-J. *Chem. Rev.* **1990**, *90*, 1359−1376.

(53) Soda, T.; Kitagawa, Y.; Onishi, T.; Takano, Y.; Shigeta, Y.; Nagao, H.; Yoshioka, Y.; Yamaguchi, K. *Chem. Phys. Lett.* **2000**, *319*, 223−230.

(54) Law, N. A.; Kampf, J. W.; Pecoraro, V. L. *Inorg. Chim. Acta* **2000**, *297*, 252−264.

(55) Wieghardt, K.; Bossek, U.; Bonvoisin, J.; Beauvillain, P.; Girerd, J. J.; Nuber, B.; Weiss, J.; Heinze, J. *Angew. Chem., Int. Ed. Engl.* **1986**, *25*, 1030−1031.

(56) Cooper, S. R.; Calvin, M. *J. Am. Chem. Soc.* **1977**, *99*, 6623−6630.

(57) Cooper, S. R.; Dismukes, G. C.; Klein, M. P.; Calvin, M. *J. Am. Chem. Soc.* **1978**, *100*, 7248−7252.